

Optimization and validation of a LaBr₃ (Ce) detector model for use in Monte Carlo simulations

Hasan, M.M.; Vidmar, T.; Rutten, J.; Verheyen, L.; Camps, J.; Huysmans, M.

Published in:
Applied Radiation and Isotopes

DOI:
[10.1016/j.apradiso.2021.109790](https://doi.org/10.1016/j.apradiso.2021.109790)

Publication date:
2021

License:
CC BY-NC-ND

Document Version:
Accepted author manuscript

[Link to publication](#)

Citation for published version (APA):

Hasan, M. M., Vidmar, T., Rutten, J., Verheyen, L., Camps, J., & Huysmans, M. (2021). Optimization and validation of a LaBr₃ (Ce) detector model for use in Monte Carlo simulations. *Applied Radiation and Isotopes*, 174, [109790]. <https://doi.org/10.1016/j.apradiso.2021.109790>

Copyright

No part of this publication may be reproduced or transmitted in any form, without the prior written permission of the author(s) or other rights holders to whom publication rights have been transferred, unless permitted by a license attached to the publication (a Creative Commons license or other), or unless exceptions to copyright law apply.

Take down policy

If you believe that this document infringes your copyright or other rights, please contact openaccess@vub.be, with details of the nature of the infringement. We will investigate the claim and if justified, we will take the appropriate steps.

Optimization and validation of a $\text{LaBr}_3(\text{Ce})$ detector model for use in Monte Carlo simulations

Md Moudud Hasan^{1,2*}, Tim Vidmar¹, Jos Rutten¹, Leen Verheyen¹, Johan Camps¹, Marijke Huysmans²

¹SCK CEN, Belgian Nuclear Research Centre, Boeretang 200, BE-2400, Mol, Belgium

²Department of Hydrology and Hydraulic Engineering, Vrije Universiteit Brussel (VUB),
Pleinlaan 2, BE-1050, Brussels, Belgium

*Corresponding author email: hasanmoudud@gmail.com

Abstract

A reliable detector model is needed for Monte Carlo efficiency calibration. A LaBr₃(Ce) detector model was optimized and verified using different radioactive sources (²⁴¹Am, ¹³³Ba, ¹³⁷Cs, ⁶⁰Co and ¹⁵²Eu) and geometries (point, extended and surface). PENELOPE and MCNP were used for Monte Carlo simulations. A good agreement was observed between simulated and experimental full energy peak efficiencies (FEPE) as their mean relative difference was $2.84\% \pm 1.93\%$ and $2.79\% \pm 1.99\%$ for PENELOPE and MCNP simulation, respectively. The differences between simulated FEPEs of two Monte Carlo codes were negligible except for low energies (< 100 keV).

Keywords: Monte Carlo, Lanthanum bromide, Gamma spectrometry, MCNP, PENELOPE

1. Introduction

Gamma spectrometry is a well-known method of identifying and quantifying the gamma emitting radionuclides in a sample in laboratory conditions as well as in situ in the field. Gamma spectrometry in a controlled environment of a laboratory is the standard way of measuring the activities of radionuclides present in a sample. On the other hand, in situ measurements are preferred to characterize a wider area, especially to avoid the laborious process of collecting numerous samples which can be expensive and time-consuming as well as unrepresentative (IAEA, 2003; Miller and Shebell, 1993; Tyler, 2008). Different types of gamma detectors are available on the market for gamma spectrometry. Among those, a High-Purity Germanium (HPGe) detector is preferred for its high energy resolution. However, a HPGe detector requires a cooling system, and a high-efficiency detector can be relatively expensive. Such limitation (cooling system or price) of a HPGe detector could limit its application for in situ measurements (Cinelli et al., 2016). On the other hand, inorganic scintillation detectors such as *NaI*, *LaBr₃(Ce)* do not need a cooling system and require a relatively short counting time, thanks to their high detection efficiencies (Tain et al., 2015). However, they have some drawbacks as well, such as a lower energy resolution than their HPGe counterparts and a temperature dependency influencing the energy calibration.

A Lanthanum Bromide scintillation (*LaBr₃(Ce)*) detector has some improved properties such as higher energy resolution, larger intrinsic efficiency and faster scintillation time response in comparison to *NaI(Tl)* detectors (Van Loef et al., 2002). However, it has some limitations as well, such as its intrinsic activity due to the presence of the long-lived ¹³⁸*La* and ²²⁷*Ac* radioisotope, and its relatively higher price compared to *NaI(Tl)* detectors because of its complicated manufacturing process (Knoll, 2010; Milbrath et al., 2007; Mouhti et al., 2018; Saizu and Cata-Danil, 2011). The intrinsic activity of a *LaBr₃(Ce)* detector is a major limitation in the case of its use in environmental monitoring, especially for low activity samples when the count rate of the sample is low compared with the count rate from the internal activity of the detector. However, in such cases, it is often useful to subtract an energy-calibrated background spectrum from the measured spectra to get the counts of a low activity sample. On the other hand, a lightweight portable *LaBr₃(Ce)* detector can be developed because of its high detection efficiency. Such a portable detector can be a preferred option for gamma spectrometry in a variety of cases, such as measurements in a borehole (Kastlander and Bargholtz, 2011; Wu and Tang, 2012), characterization of contaminated sites (Ji et al., 2019; Varley et al., 2017, 2015), in a marine environment (Zeng et al., 2017), for

various monitoring measurements in nuclear plants (Garnett et al., 2017; Urban and Vágner, 2019) and unmanned aerial vehicle (UAV) aviation radiation monitoring (Tang et al., 2016).

The full energy peak efficiency (FEPE) for the energy of interest is required to calculate the activity concentration of radionuclides in a sample. The FEPE can be determined experimentally as well as mathematically. The experimental FEPE determination, known as efficiency calibration, requires the reference materials with known activities and identical geometries as the sample to be measured (Daza et al., 2001; Iurian and Cosma, 2014; Rizwan et al., 2015; Shizuma et al., 2016). It is expensive and challenging to do experimental calibrations as the source distribution and measurement conditions vary a lot, especially in the case of in situ measurements (Guerra et al., 2018; Mairing et al., 2018). An efficient alternative to the experimental calibration is the Monte Carlo simulations of the detector efficiency.

Monte Carlo methods are often used to calibrate and analyze the efficiency of a radiation detector (Anil Kumar et al., 2009; Ciupek et al., 2014; Mouhti et al., 2018; Sahiner and Liu, 2020; Su et al., 2011; Tain et al., 2015; Wu and Tang, 2012; Zeng et al., 2017). It can be used to calculate the detector efficiency for a wide variety of geometries and distributions of the radioactive sources which are difficult to do experimentally (Boson et al., 2009). Several computer codes can be used for Monte Carlo simulation such as MCNP6 (Goorley et al., 2013), GEANT4 (Agostinelli et al., 2003), PENELOPE (Baró et al., 1995), FLUKA (Ferrari et al., 2005), EGS5 (Hirayama et al., 2005). These computer codes can simulate the radiation transport and interaction processes of photons and electrons in an arbitrary material (Jung et al., 2018; Ordóñez et al., 2019; Vidmar et al., 2008). There are also several commercial software available for numerical simulation of gamma detectors, such as LabSOCS (Bronson, 2003), ISOCS (Canberra, 2017), ANGLE (Jovanovic et al., 2010), etc.

A detector model used in Monte Carlo simulation should mimic the characteristics of the real detector to obtain reliable FEPEs. A reliable detector model can be obtained by optimizing its parameters based on measured efficiencies of calibrated standards in laboratory conditions, with which the computed efficiencies are compared. In laboratory conditions, the sources are always closer to the detector than in field measurements, making the model of the measurement setup, including the detector itself, more sensitive to the values of its parameters. The optimized detector model can then be validated by measuring additional standards that were not used in the optimization process. Such a procedure, if carried out

properly, can be expected to be reliable to yield a detector model suitable for efficiency computation of in situ measurement geometries.

Anil Kumar et al. (2009) have obtained good agreement between experiments and Monte Carlo simulations using the GEANT4 code for the efficiency calibration of a 25.4 mm × 25.4 mm cylindrical $LaBr_3(Ce)$ detector using calibrated point sources of ^{137}Cs and ^{60}Co . A 50.8 mm × 50.8 mm $LaBr_3(Ce)$ detector model was validated using two different Monte Carlo codes, EGS5 by Casanovas et al. (2012) and MCNP by Mouhti et al. (2018). The simulated efficiencies vary by 10 to 20% between the two codes, depending on the gamma energies. Karfopoulos and Anagnostakis (2010) have analyzed the effect of various simulation parameters on the full energy peak efficiency determination of a HPGe detector. They recommended that simulation parameters (e.g., the energy bin width, the cut-off energy for photons and electrons, the photo-peak bin upper and lower limits) be carefully selected to get accurate results and to optimize the simulation speed. A wrong simulation parameter may lead to an unrealistic detector model. However, there could be some differences in the simulated results between different codes based on the photo-atomic database and electromagnetic physics models used by the simulation codes (Jung et al., 2018).

The development of a detector model can be challenging in case of insufficient information about the detector crystal and its housing. In that case, unknown parameters of the detector can be optimized by comparing the Monte Carlo simulation and the experimental efficiency of the detector (Guerra et al., 2018, 2017; Murphy et al., 2020). As the simulated efficiency of a detector relies on many simulation parameters, it is prudent to validate the detector model using different Monte Carlo codes. Moreover, it is also necessary to validate the detector model using different types of sources such as point sources and extended sources, as well as for different energies. Hurtado and Villa (2010) found a higher discrepancy for extended sources than for point sources between the experimental and the simulated efficiency for a HPGe detector.

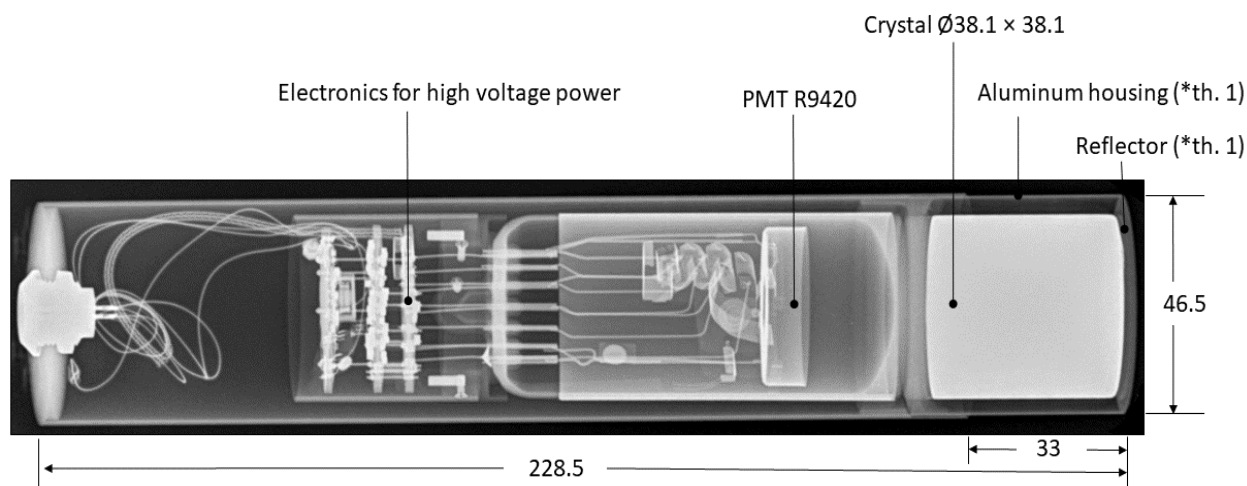
In this study, we optimized and verified a $LaBr_3(Ce)$ detector model using point sources and extended sources. We used two different Monte Carlo codes, namely PENELOPE and MCNP. The ultimate objective is to use this verified model for in situ efficiency calibration. Therefore, an in situ measurement scenario was also created using surface sources. We compared the simulated efficiencies between the codes.

2. Materials and methods

2.1. Experimental setup

A 38.1 mm × 38.1 mm cylindrical $LaBr_3(Ce)$ detector (Model 38S38/1.5/HV) coupled with a photo-multiplier tube (PMT) (Model R9420), produced by Saint-Gobain (Saint-Gobain, 2020), was used in this study. The resolution of the detector is $\leq 3.5\%$ at 662 keV. Due to the internal contaminants (^{138}La and ^{227}Ac), several peaks can be observed in the background spectrum such as a peak at approximately 1468 keV due to the 1436 keV gamma-ray from ^{138}La with a coincident X-ray, and several peaks between 1850 and 3000 keV that are associated with the alpha decays from ^{227}Ac . In addition, a broad feature can be found in the background spectrum at 750–1000 keV because of the 789 keV gamma-ray in coincidence with a beta particle (Milbrath et al., 2007). This internal contamination can be problematic for low counting applications of large $LaBr_3(Ce)$ detectors.

An X-ray image of the detector shows its internal configuration (Figure 1). The SAM 940 (BNC, 2007), a portable radio-isotope identification system, was used to operate the detector. A computational model of the detector was developed based on an X-ray image and a technical drawing obtained from the manufacturer. The computational detector model was further optimized based on the experimental FEPEs. Therefore, the first step was to get experimental FEPEs. Hence, certified point sources and extended sources were measured (Table 1). Those sources were prepared and certified by the Gamma-spectrometry Laboratory of the Belgian Nuclear Research Center (SCK CEN). Point sources of the radionuclides ^{241}Am , ^{137}Cs , ^{152}Eu and ^{60}Co were used in this experiment. The point sources were in the center of a plastic disc of 1.5 cm diameter and 3 mm thickness. The point sources were measured at three different distances (0, 5 and 10 cm) from the top of the detector window and the side of the detector. Four extended sources were also used in this experiment. Those four extended sources were all water solutions (liquid) of the radionuclides ^{241}Am , ^{133}Ba , ^{137}Cs and ^{60}Co , respectively. The water solutions were poured into a High-Density Polyethylene (HDPE) container with an outer diameter of 6.16 cm, a wall thickness of 0.68 mm and a bottom thickness of 1.58 mm. The filling height of the water solution sources was 8.83 cm. During the measurements, the plastic container with the water solution was placed directly on top of the detector window. The live time of the measurement was preset to 900 seconds to keep the net peak area uncertainty low ($\leq 1\%$).



*th. = thickness

Figure 1. X-ray image of the detector. (Unit: mm).

Table 1. Characteristics of the radioactive sources used in this work. Uncertainties are presented as two times the standard deviation ($k=2$).

Nuclide	Activity (Bq)	Type	Measurement setup
^{241}Am	40268 ± 604	Point	0, 5 and 10 cm from the top and side of the detector window.
^{60}Co	8816 ± 75		
^{137}Cs	30175 ± 302		
^{152}Eu	1491 ± 20		
^{241}Am	8421 ± 198	Extended	Water solution in HDPE container on top of the detector window.
^{60}Co	7048 ± 328		
^{137}Cs	3067 ± 94		
^{133}Ba	3666 ± 113		
^{137}Cs	219614 ± 1760	Surface	The detector was 1 m above a $3.15 \text{ m} \times 2.97 \text{ m}$ surface source.
^{133}Ba	92918 ± 726		

2.2. Calculation of experimental FEPEs

The experimental FEPEs were calculated for the following photon energies (all given in keV): 59 (^{241}Am), 121 (^{152}Eu), 244 (^{152}Eu), 344 (^{152}Eu), 662 (^{137}Cs), 1173 (^{60}Co) and 1332 (^{60}Co) for point sources, and 59 (^{241}Am), 81 (^{133}Ba), 303 (^{133}Ba), 356 (^{133}Ba), 662 (^{137}Cs),

1173 (^{60}Co) and 1332 (^{60}Co) for extended sources. The experimental FEPEs were calculated using equation (1), and their uncertainties (u_{FEPE}) were determined using equation (2). In those equations, N stands for the net counts observed in the relevant full energy peak, A for the activity in Bq of the relevant radionuclide, P_γ for the corresponding probability of the gamma emission, t for the acquisition live time in seconds, C_s for the coincidence-summing correction factors. The u_N , u_A and u_p are the corresponding uncertainties of N , A and P_γ , respectively. The uncertainty on t and C_s was negligible compared to other uncertainties entering the equation, so it was not included in the calculation. Notations are according to Guerra et al. (2018). The values of P_γ and its uncertainties were obtained from the database of the Bureau International des Poids et Mesures (BIPM) (Bé et al., 2010, 2006). The factor C_s was calculated using EFFTRAN (Vidmar et al., 2011).

$$FEPE = \frac{N}{A \cdot P_\gamma \cdot t} \cdot C_s \quad (1)$$

$$u_{FEPE} = FEPE \sqrt{\left(\frac{u_N}{N}\right)^2 + \left(\frac{u_A}{A}\right)^2 + \left(\frac{u_{P_\gamma}}{P_\gamma}\right)^2} \quad (2)$$

The net counts (N) and standard deviation of net counts (u_N) in the peak area were calculated using equation (3) and equation (4) (Gilmore, 2008):

$$N = \sum_{i=L}^U N_i - n \left(\sum_{i=L-m}^{L-1} N_i + \sum_{i=U+1}^{U+m} N_i \right) / 2m \quad (3)$$

$$u_N = \sqrt{\sum_{i=L}^U N_i + n^2 \left(\sum_{i=L-m}^{L-1} N_i + \sum_{i=U+1}^{U+m} N_i \right) / 4m^2} \quad (4)$$

Here, N_i is the counts in the i^{th} channel of the measured spectrum, and L and U are respectively the lower and the upper channel number of the peak region. By n , the number of channels within the peak region is designated, and m is the number of channels selected on each side of the peak region to estimate the background below the peak. The location and ROI of the peak were estimated using the MultiSpect Analysis software (MultiSpect, 2018) of Kromek Limited.

2.3. Monte Carlo simulation

2.3.1. Monte Carlo codes

We used two different Monte Carlo codes in this study, namely PENELOPE (PENetration and Energy Loss Of Positrons and Electrons) (Salvat, 2019) and MCNP (Monte Carlo N-Particle) (Goorley et al., 2013). Both codes simulate the transport of electrons and photons based on the Monte Carlo method. Users have control over the parameters of the computational model such as geometry, chemical composition and density of the materials.

PENELOPE version-2018 (PENELOPE-2018) (Salvat, 2019) was used in this study. It consists of a set of subroutines written in FORTRAN. It simulates the coupled electron-photon transport in any material for energies between 50 eV and 1 GeV. The photoelectric cross sections database of PENELOPE-2018 was calculated with the FORTRAN program *PHOTACS* by Sabbatucci and Salvat (2016). This program is based on the same theory used for the Evaluated Photon Data Library (EPDL) tables by Scofield (1973), but implements more accurate numerical algorithms (Salvat, 2019). The Penmain.f subroutine of PENELOPE was used for the simulation of the detector. This code requires the information contained in several input files such as the geometry file, material files, main input file which contains the source definition, the detector definition.

MCNP6.1 (cloud version) was used in this study (Goorley et al., 2013). In MCNP, we used the default photo-atomic library-MCPLIB84 (White, 2012). This photo-atomic library contains information on photon interactions for elements from $Z = 1$ to 100 with energy as low as 1 keV (Goorley et al., 2013; Jung et al., 2018). The difference between the photo-atomic database of MNCP and PENELOPE may lead to an imperfect match between the simulated efficiencies.

2.3.2. Simulation parameters and FEPE calculation

206 Sources of mono-energetic photons were used to simulate the FEPE of a given sample-
 207 detector configuration. Some of the well-known gamma lines of natural and artificial
 208 radionuclides were used in this study. These photon energies (in keV) and the emitting
 209 radionuclides (in parenthesis) are 59 (^{241}Am), 81 (^{133}Ba), 109 (^{235}U), 121 (^{152}Eu), 186 (^{235}U),
 210 244 (^{152}Eu), 303 (^{133}Ba), 344 (^{152}Eu), 356 (^{133}Ba), 583 (^{208}Tl), 662 (^{137}Cs), 768 (^{214}Bi), 911
 211 (^{228}Ac), 1173 (^{60}Co), 1332 (^{60}Co), 1461 (^{40}K), 1764 (^{214}Bi) and 2614 (^{208}Tl). In both codes, the
 212 cutoff energy for particle tracking was set to 1 keV for both electrons and photons, as the
 213 default photo-atomic library (MCPLIB84) in MCNP does not support a cutoff below 1 keV
 214 (Goorley et al., 2013). However, the latest versions 6.1 and 6.2 of MCNP give the possibility
 215 to specify a lower cutoff energy down to 1 eV using an updated photo-atomic library
 216 EPRDATA12 and the library EPRDATA14, respectively (Goorley et al., 2013; Werner et al.,
 217 2017). For our study, using a 1 keV cutoff energy produced the required level of accuracy.
 218 The photon and electron mode (MODE P E) was used in MCNP which is a default setting in
 219 PENELOPE. The energy bin width was kept equal in both codes where 1000 bins were used,
 220 and the last bin referred to the energy equal to the maximum simulated source energy plus 10
 221 keV to avoid round-off effects. The density and chemical composition of different materials
 222 was kept the same in both codes. The details of the simulated materials are shown in Table 2.
 223 The geometry of all simulations was carefully checked, to ensure that the same dimensions
 224 were used in both codes. For point and extended source simulations, 10^8 primary particles
 225 were simulated to keep the statistical uncertainty below 0.5%. In MCNP, the pulse height tally
 226 (known as F8) was used to calculate the FEPE of the respective photon energy. In
 227 PENELOPE, the energy deposition type tally was used, and the FEPE was calculated using
 228 equation (5).

$$FEPE_{PEN} = N_i \cdot W_{bin} \quad (5)$$

229 Here, N_i is the probability density of deposited energy per particle ($1/(eV \times particle)$) of i^{th}
 230 energy bin and W_{bin} is the energy bin width in eV.

231 Table 2. Materials used in the simulation with their chemical composition and density.

Material			
no.	Material name	Chemical composition	Density ($g\ cm^{-3}$)
1	Air	$N(0.78)\ O(0.21)\ Ar(0.0046)\ C(0.00015)^*$	0.001205

2	Detector Crystal	$LaBr_3$	5.08
3	Photo Multiplier Tube	SiO_2	2.60
4	PTFE Reflector	$(C_2F_4)_n$	2.20
5	Aluminum	Al	2.69
6	High Density Polyethylene (HDPE)	$(CH_2)_n$	0.94
7	Water	H_2O	1.00

232 * Weight fraction

233 2.4. Detector model

234 From the physical dimensions and the manufacturer's information, the dimensions of the
235 detector were estimated as shown in Figure 1 and Figure 2. The detector crystal is cylindrical
236 with a 38.1 mm diameter and a 38.1 mm height. We do not have the exact information about
237 the distance between the detector crystal and the aluminum window top of the detector. From
238 the X-ray image, it can be estimated that this distance is between 1 and 3 mm. However, we
239 know there is a 1 mm Polytetrafluoroethylene (PTFE) reflector surrounding the crystal.
240 Therefore, this distance should be at least 1 mm, and it was optimized using experimental
241 FEPEs as described in section 2.5. The computational detector model is shown in Figure 2.
242 The chemical composition and density of the materials used in the detector model are given in
243 Table 2. The glass body of the photo-multiplier tube (PMT) was also included in the model.
244 However, the electronics were not included in the model, and the effect of the PMT and the
245 electronics on the efficiency is negligible for the sources located on the opposite side of the
246 detector crystal (Mouhti et al., 2018, 2017).

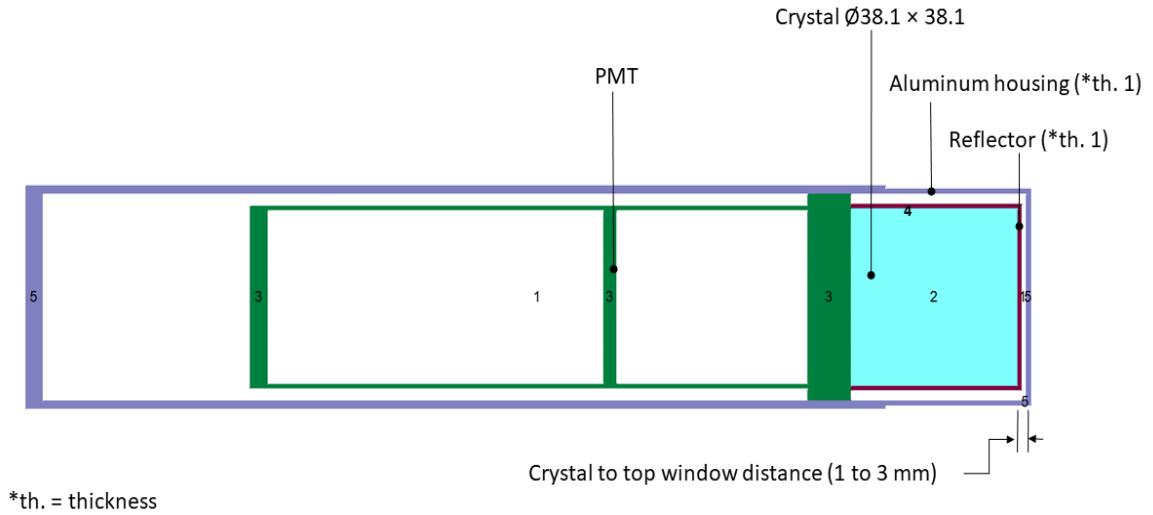


Figure 2. Model of the detector used in the simulation (image not to scale). The colors represent different materials and the labels correspond to the material numbers of Table 2. (Unit: mm)

2.5. Detector model optimization

The gap between the detector crystal and the top aluminum window was optimized using the experimental FEPE of the point sources placed on top of the aluminum window. Other parameters of the detector model, such as the diameter and length of the crystal, were kept as read out from the manufacturer's specifications and the X-ray image. This approach is justified by the satisfactory agreement between the measured and calculated FEPEs, but also by the fact that machining the crystals is generally a very accurate operation.

Point sources were preferred for the measurements because this type of sources can be positioned close to the detector, and the related FEPEs are therefore more sensitive to the size of the air gap compared to extended sources. In addition, the uncertainty due to source positioning could be avoided. Four experimental FEPEs were used in this optimization process. These FEPEs were obtained from the point sources of 59 keV of ^{241}Am , 662 keV of ^{137}Cs , 1173 and 1332 keV of ^{60}Co . As we used a ^{60}Co source in this optimization process, we needed to determine the corresponding coincidence summing correction factors to calculate the experimental FEPEs. The calculation of coincidence summing correction factors is described in section 2.6. For the optimization of the detector model, PENELOPE was used since we have limited access to the MCNP cloud version for the automation of the optimization process.

The objective function to be minimized is the sum of the quadratic relative differences between the FEPEs calculated by simulation, and the set of experimental FEPEs, and is given by equation (6) (Guerra et al., 2015):

$$f_{opt}(x) = \sum_{i=1}^{i=n} \left(\frac{FEPE_{Calculated}(E_i, x) - FEPE_{Experimental}(E_i)}{FEPE_{Experimental}(E_i)} \right)^2 \quad (6)$$

Where n is the number of different FEPEs, E_i is the energy of i^{th} FEPE, $FEPE_{Calculated}(E_i, x)$ is the calculated efficiency from simulation corresponding to the parameter set x of the detector model and energy E_i , and $FEPE_{Experimental}(E_i)$ is the experimental FEPE for a photo-peak with energy E_i .

A Python (Python, 2020; Van Rossum and Drake, 2011) script was written for this optimization process. The script generates geometry files using the parameter values provided by the minimization function. Then, PENELOPE simulations were run for the above-mentioned four sources, and the FEPEs were calculated. The value of the objective function was calculated using equation (6). The optimization function evaluates the value of the objective function, and either provides new parameter values for the next iteration or terminates the calculation if the optimum result is obtained. The “*scipy.optimize.fmin*” is an optimization function from the SciPy library (Virtanen et al., 2020) that we used to minimize the objective function. This minimization function uses the Nelder-Mead simplex algorithm (Nelder and Mead, 1965) to find the minimum of a function of one or more variables. During the optimization, the simulation times for each run were typically 15 minutes for the 59 keV and 662 keV sources and 25 minutes for the 1173 keV and 1332 keV gamma lines.

2.6. Coincidence summing correction factors

The value of coincidence summing correction factor (C_s) of the 1173 and 1332 keV photon energies emitted in the decay of ^{60}Co were calculated via the EFFTRAN code (Vidmar et al., 2011). This factor depends on different parameters of the detector and source. During the optimization process, we optimized only one parameter of the detector, the distance between the crystal and the window, and we needed a model to calculate the C_s as a function of this distance. Hence, the C_s of the 1173 and 1332 keV gamma lines of ^{60}Co for different air gaps from 1 mm to 3 mm was calculated from EFFTRAN (Vidmar et al., 2011). From these data, two different linear models were constructed for 1173 and 1332 keV photon energies as shown in Figure 3. These linear models were used in the optimization process to calculate the coincidence summing correction factors for the different air gaps.

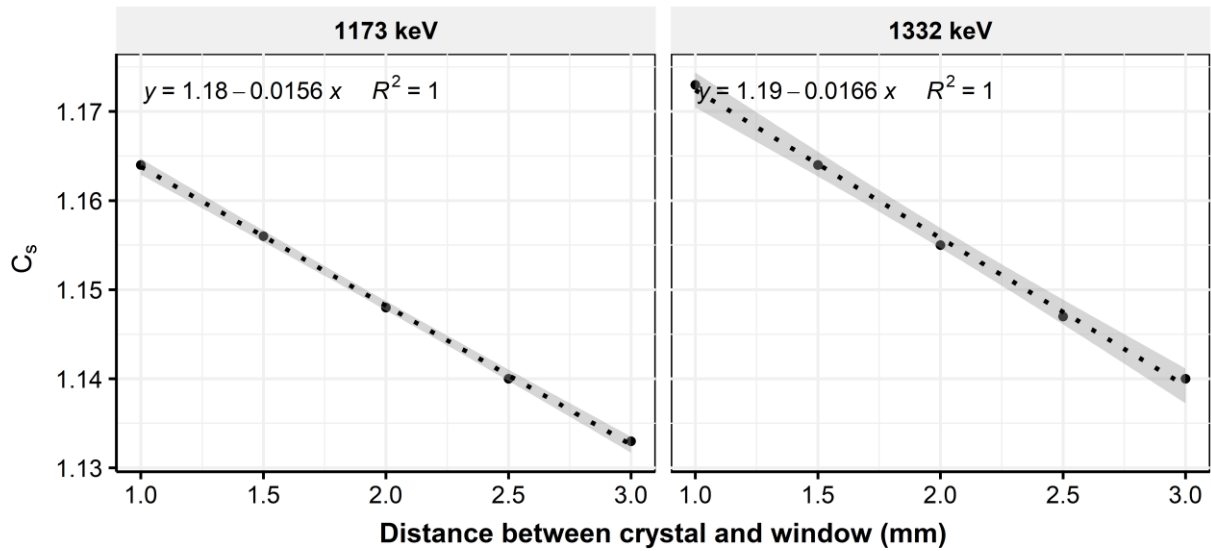


Figure 3. Coincidence summing correction factors for ^{60}Co as a function of the distance between the detector crystal and the window.

2.7. Validation of the detector model

The optimized detector model was verified using geometries and sources different from those used in the optimization process. The experimental setup of both point sources and extended sources at different distances from the detector window were simulated separately using PENELOPE and MCNP. An illustration of the geometry used in the simulation of point sources and an extended source is shown in Figure 4(a) and Figure 4(b), respectively. The dimensions of these sources are given in section 2.1. In the case of an extended source, the points of origin of the emitted gamma rays were assumed to be uniformly distributed over the source volume.

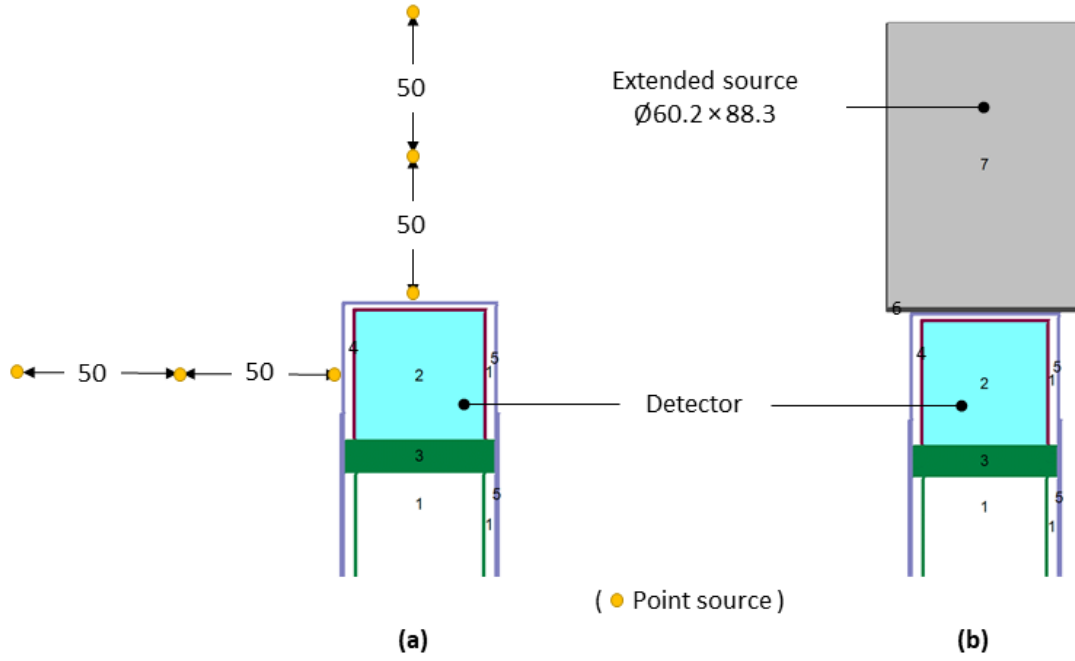


Figure 4. Illustration of the geometry used in the simulation of (a) point sources at 0, 5 and 10 cm from the top and side of the detector window and (b) an extended source on top of the detector window (images not to scale). The colors represent different materials, and the numbers correspond to the material numbers in Table 2. (Unit: mm).

The calculated FEPEs were compared with experimental FEPEs to evaluate the performance of the detector model. The evaluation of the model performance was carried out based on the ratio between calculated and experimental FEPEs (equation (7)) and the zeta-score (equation (8)), also known as the *u-test* (Guerra et al., 2018). The percentage of relative difference (RD) between the FEPE of PENELOPE ($FEPE_{PENELOPE}$) and MCNP ($FEPE_{MCNP}$) was calculated using equation (9).

$$Ratio = \frac{FEPE_{Calculated}}{FEPE_{Experimental}} \quad (7)$$

$$zeta \text{ score} = \frac{|FEPE_{Calculated} - FEPE_{Experimental}|}{\sqrt{u_{FEPE_{Calculated}}^2 + u_{FEPE_{Experimental}}^2}} \quad (8)$$

$$RD = \frac{|FEPE_{PENELOPE} - FEPE_{MCNP}|}{\left(\frac{FEPE_{PENELOPE} + FEPE_{MCNP}}{2}\right)} \times 100 \quad (9)$$

324

325 2.8. Detector model validation for an in situ scenario

326 Detector's performance was also evaluated for surface sources, which is similar to an in situ
 327 measurement setup one would encounter in the field. Usually, in an in situ measurement, a
 328 detector is kept 1 m above the contaminated field. In such a setup, the effective source volume
 329 in the simulation can be modeled as a cylindrical slab varying in diameter from a few meters
 330 to hundreds of meters, and in depth from a few centimeters to a few meters, depending on the
 331 photon energy and density of the soil (Androulakaki et al., 2016; Chiroasca et al., 2013;
 332 Rostron et al., 2014; Zhang et al., 2015). The effective volume is the minimum volume for
 333 which the volumetric detection efficiency reaches a plateau. In this experiment, a 9.36 m²
 334 (3.15 m × 2.97 m) surface area source (Table 1) was used with a detector placed in the middle
 335 at 1 m above it. The surface source was a combination of ¹³³Ba and ¹³⁷Cs radionuclides
 336 uniformly distributed over 25 pads. These radioactive source pads were spread over a
 337 concrete slab. Figure 5(a) shows the setup used in this experiment, and the geometry used in
 338 the simulation is shown in Figure 5(b). The experimental FEPEs were obtained for the 356
 339 (¹³³Ba) and 662 (¹³⁷Cs) keV photon energy. The peak area of the low photon energy (81 keV
 340 of ¹³³Ba) was not significant, and therefore, experimental FEPEs of low energy were not
 341 included in the analysis. The photon energies used in the simulation were 59 (²⁴¹Am), 81
 342 (¹³³Ba), 109 (²³⁵U), 121 (¹⁵²Eu), 186 (²³⁵U), 244 (¹⁵²Eu), 303 (¹³³Ba), 344 (¹⁵²Eu), 356 (¹³³Ba),
 343 583 (²⁰⁸Tl), 662 (¹³⁷Cs), 768 (²¹⁴Bi), 911 (²²⁸Ac), 1173 (⁶⁰Co), 1332 (⁶⁰Co), 1461 (⁴⁰K), 1764
 344 (²¹⁴Bi) and 2614 (²⁰⁸Tl) keV. The density of the concrete was 2.4 g cm⁻³. The atoms per
 345 molecule of the different elements in the simulated concrete slab were H-0.169, C-0.00142,
 346 O-0.56252, Na-0.01184, Mg-0.0014, Al-0.02135, Si-0.20411, K-0.00566, Ca-0.01867 and
 347 Fe-0.00426. The activity was assumed to be uniformly distributed on the surface of the slab,
 348 and 10⁹ particles were simulated to achieve the desired statistical uncertainty (< 0.5 %) of the
 349 computed FEPEs.

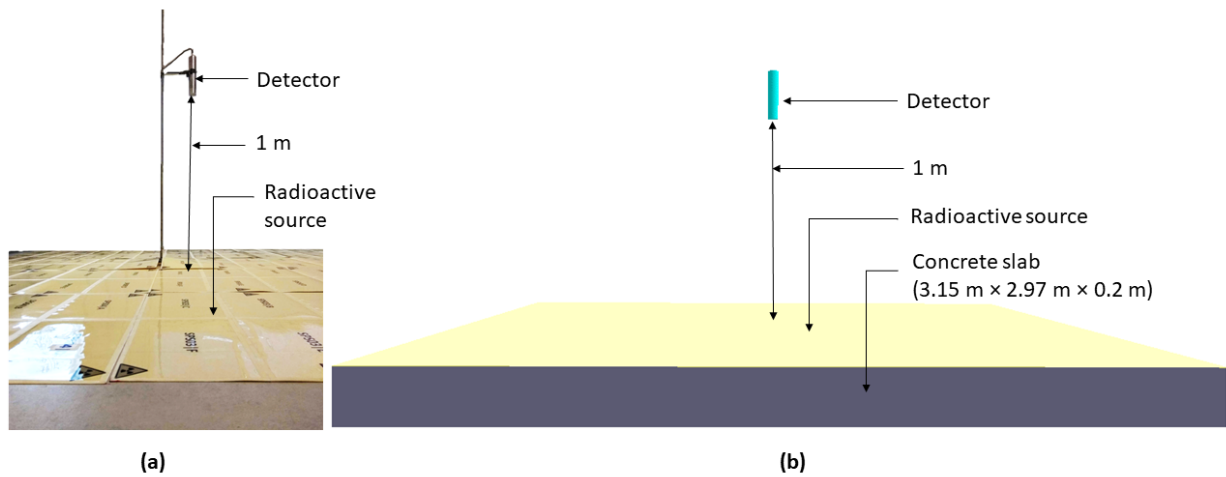


Figure 5. Illustration of the setup used for representing an in situ scenario: (a) experimental, and (b) geometry used in the simulation.

3. Results and Discussion

3.1. Optimized detector model

The result of the optimization is shown in Figure 6. The optimum solution was obtained after 13 iterations. The minimum value of the objective function was 0.0032 (red points in Figure 6). The optimum detector model was obtained for a distance of 1.9 mm between the detector crystal and aluminum window (including a 1 mm reflector). The value of the objective function increased approximately by a factor of 10 for each 1 mm change of distance from the optimum value. This indicates that the detector model is highly sensitive to the optimized parameter for point sources close to the detector.

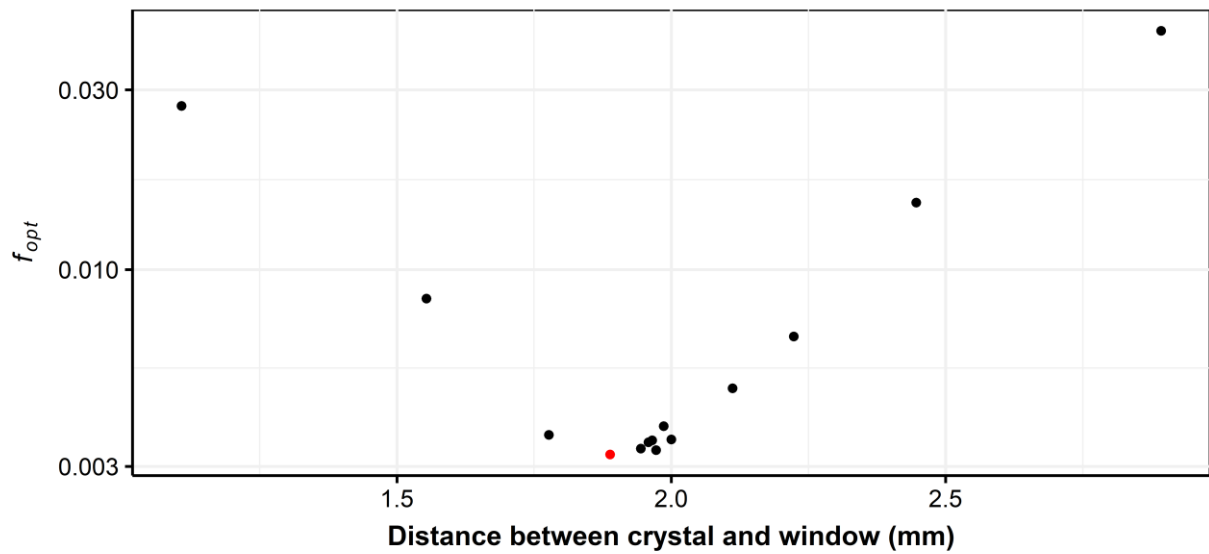


Figure 6. Value of the objective function (f_{opt}) for different distances between the detector crystal and the aluminum window. The red point is the optimal solution.

A comparison between the experimental FEPEs used in the optimization and the simulated FEPEs of PENELOPE and MCNP using the optimal model is shown in Figure 7. A good agreement between experimental and simulated FEPEs was obtained with both codes. The highest discrepancy of 5% and 6% in PENELOPE and MCNP, respectively, was obtained for 59 keV photon energy. However, all zeta scores were below 2.58 (Figure 8 (1)), which means that the experimental and simulated FEPEs did not differ significantly from each other (Shakhashiro et al., 2008). Still, there was an overestimation of the FEPE especially for low energy photons (59 keV). For a $LaBr_3(Ce)$ detector some other studies also found a larger discrepancy of 13.34% (Mouhti et al., 2018) and 5.54% (Salgado et al., 2012) for the 59 keV photon energy of an ^{241}Am source. The process of self-absorption of low energy within the source could explain this discrepancy for the low energy.

The simulated FEPE curve obtained from the PENELOPE and MCNP simulations is shown in Figure 7(a) along with their relative difference (Figure 7(c)) for the point sources positioned directly on the detector window. The experimental FEPEs are also plotted in this figure (Figure 7(a)). It was observed that the uncertainty range ($k=2$) of experimental FEPEs covered the simulated FEPEs in most of the cases. In addition, a good agreement between PENELOPE and MCNP was observed with a mean relative difference of 0.51%. The relative difference between the two codes increased with decreasing energy, particularly below 100 keV (Figure 7(c)). This difference can be caused by the differences in the photo-atomic databases and/or electromagnetic physics models used in the respective codes. Overall, a good

agreement was observed between experimental and simulated FEPEs, as well as between the codes themselves, which indicates that the detector model was well constructed and optimized.

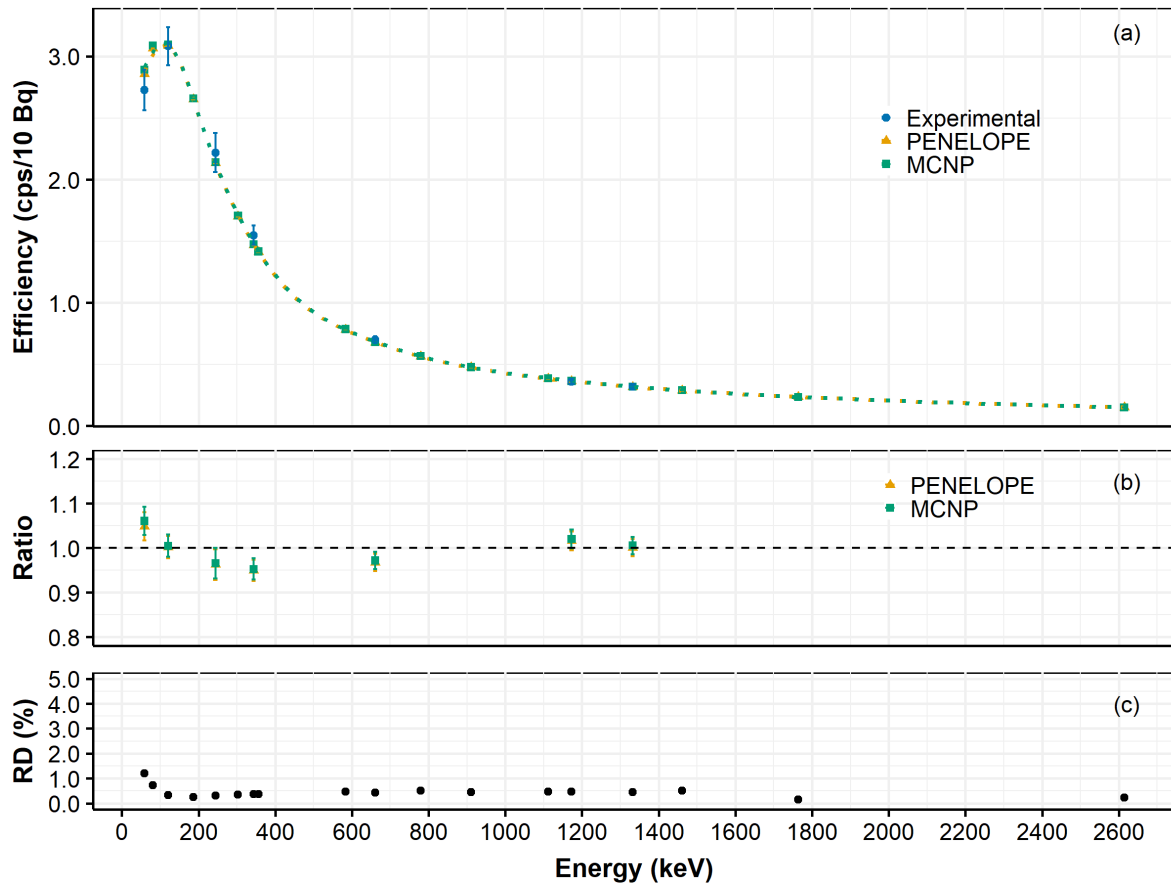


Figure 7. (a) Experimental and simulated FEPEs from PENELOPE and MCNP, (b) ratio of experimental and simulated FEPEs, and (c) relative difference (RD) between the FEPEs from PENELOPE and MCNP for point sources located on the top (0 cm) of the detector window.

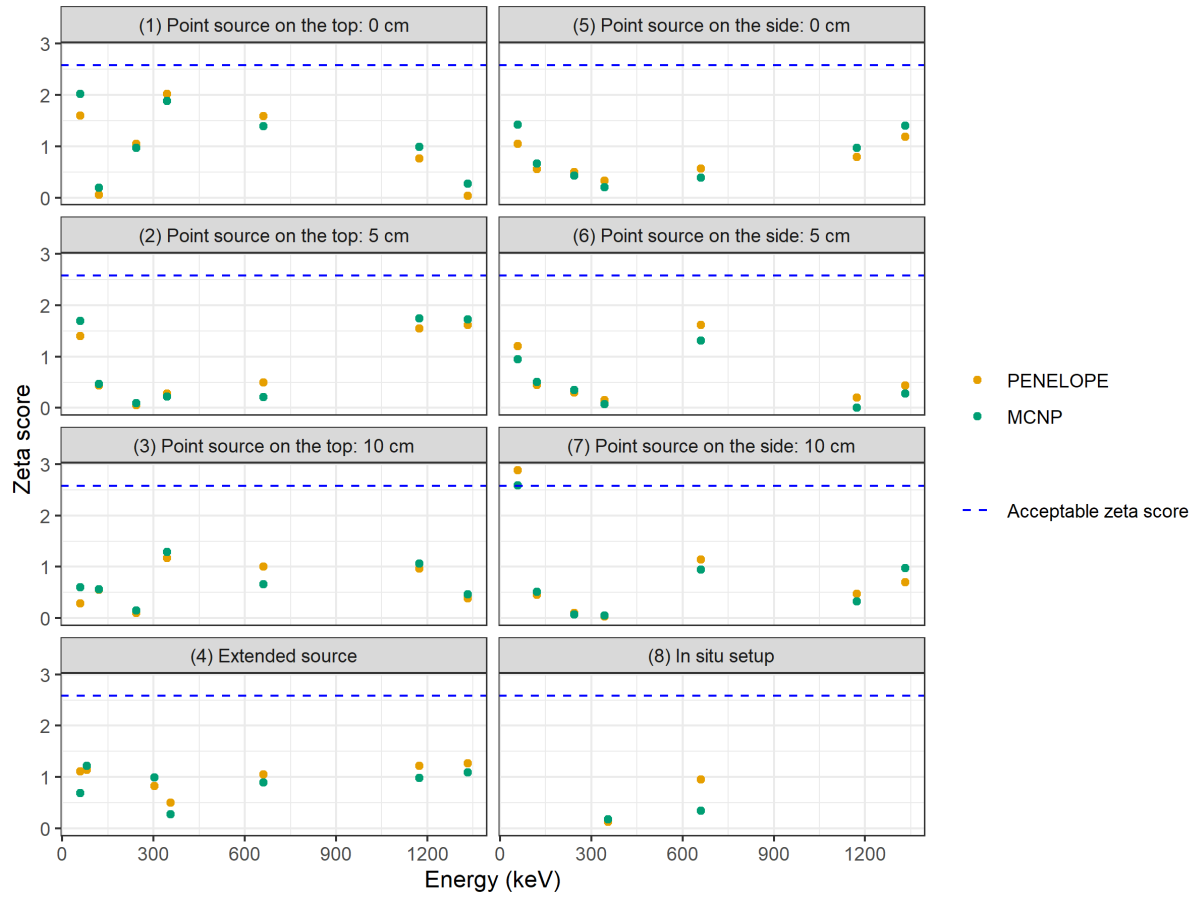


Figure 8. Zeta scores of different experimental setups.

3.2. Detector model validation

A comparison between the experimental and the simulated FEPEs obtained using the optimal model for different radioactive source geometries is given in this section.

3.2.1. Sources on the top of the detector window

The optimized detector model was validated with extended sources and point sources positioned at 5 and 10 cm from the top of the detector window. The simulated FEPE curve obtained from both codes and their relative difference for point sources at 5 cm and 10 cm and the extended sources are shown in Figure 9, Figure 10 and Figure 11, respectively. In these figures, the corresponding experimental FEPEs are plotted with their uncertainty ($k=2$). The efficiency curves shown in the figures have similar shapes with maximum efficiency at about 100 keV, and then efficiency decreased exponentially with increasing energy. It was observed that the expanded uncertainty of the experimental FEPEs covered the simulated FEPEs in all cases (Figure 9, Figure 10 and Figure 11). The mean relative difference between PENELOPE and experimental FEPEs was about 3.03% with a standard deviation of 1.62%. In the case of MCNP, the mean relative difference was about 3.04% with a standard deviation of 1.79%. In

addition, the zeta scores of both codes were well below the critical limit of 2.58 in all cases. A result with a zeta score of less than 2.58 is considered acceptable (Shakhashiro et al., 2008). Moreover, only the statistical uncertainty ($< 0.5\%$) from the simulation was considered as the uncertainty in the simulated FEPEs in the zeta score calculation. Considering the simulated FEPE uncertainty due to the uncertainty in the source-to-detector distance and the uncertainty on the material composition and density of the sample will reduce the zeta score. Overall, the results demonstrate that the optimized detector model can reliably be used to calculate the FEPEs in other geometries than the one used in the optimization process.

The mean relative difference between the two codes was 0.43% and 0.55% for point sources at 5 cm and 10 cm distance, respectively. A similar level of difference (0.57%) between the two codes was observed in the case of an extended source. Vidmar et al. (2008) found about 10% differences between different codes for lower photon energy (45 keV).

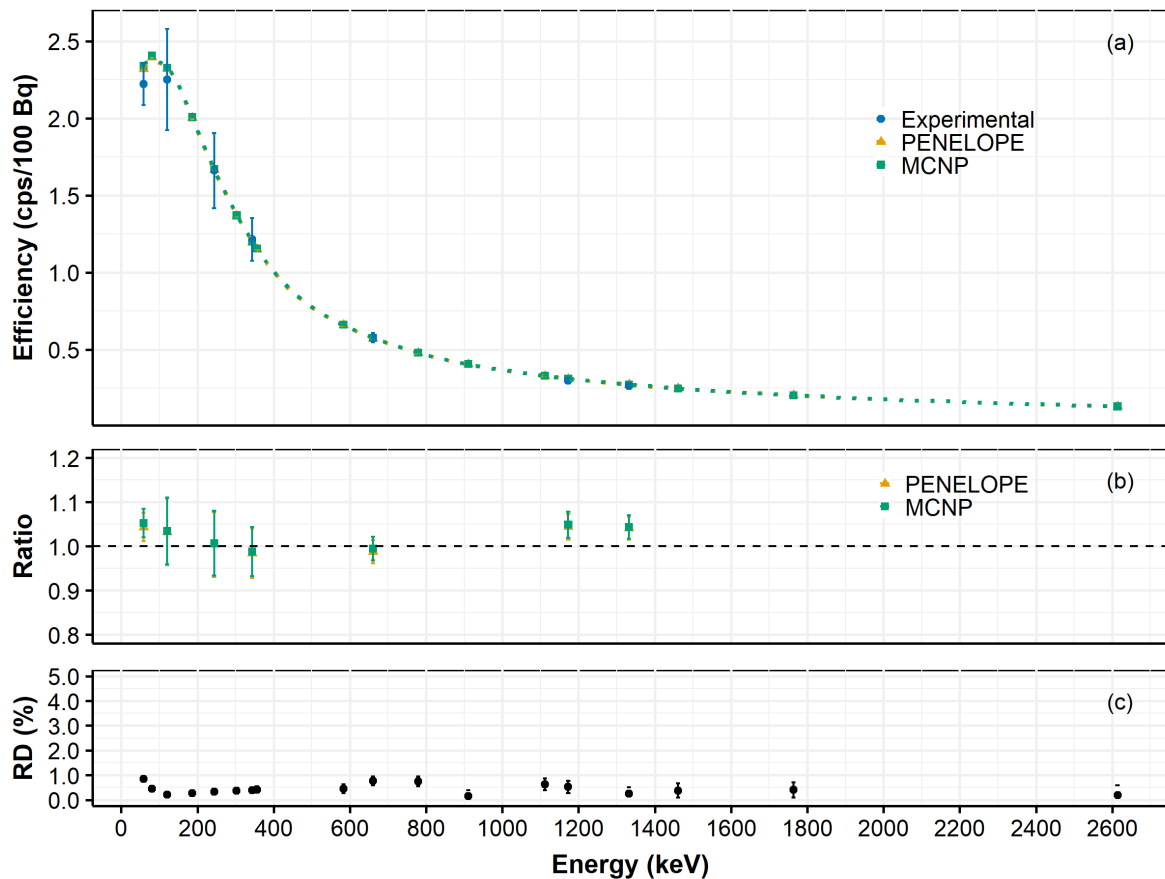


Figure 9. (a) Experimental and simulated FEPEs from PENELOPE and MCNP, (b) ratio of experimental and simulated FEPEs, and (c) relative difference (RD) between the FEPEs from PENELOPE and MCNP for point sources at 5 cm from the top of the detector window.

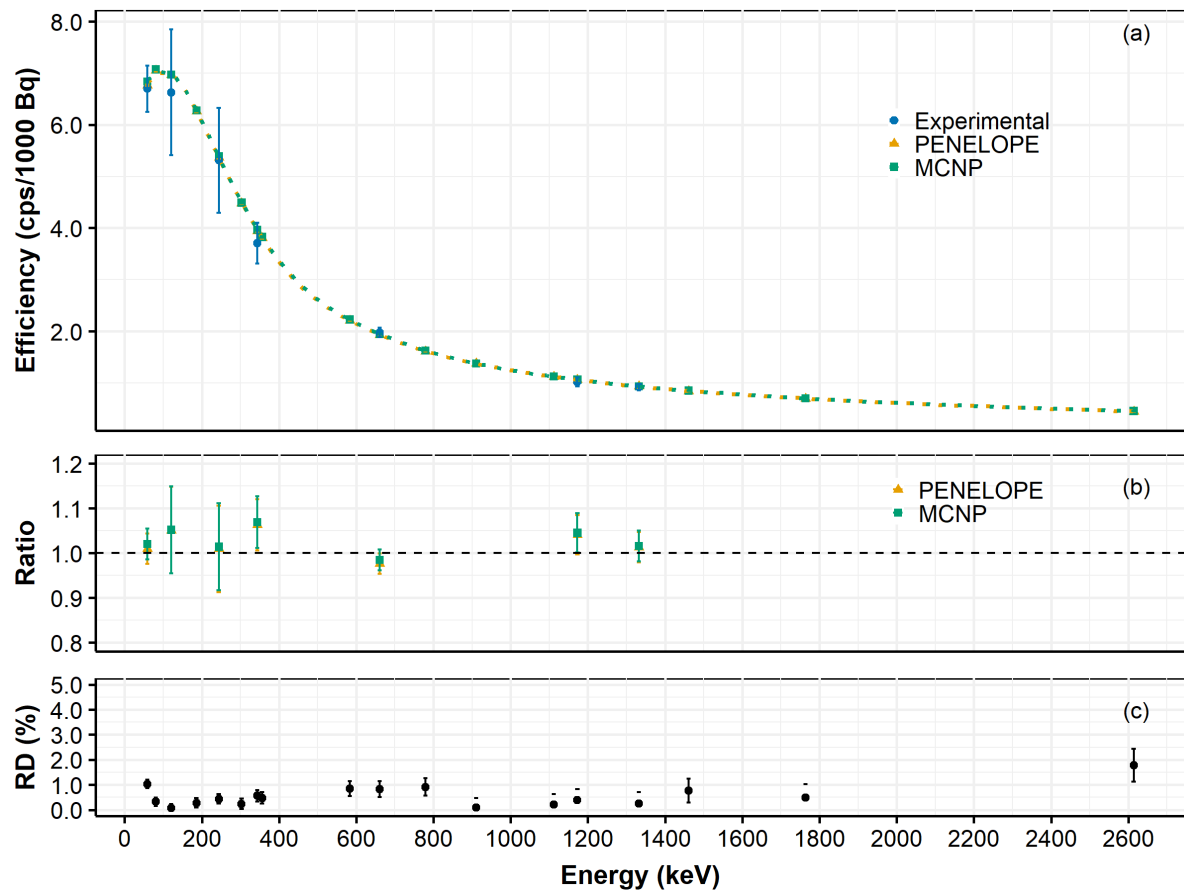


Figure 10. (a) Experimental and simulated FEPEs from PENELOPE and MCNP, (b) ratio of experimental and simulated FEPEs, and (c) relative difference (RD) between the FEPEs from PENELOPE and MCNP for point sources at 10 cm from the top of the detector window.

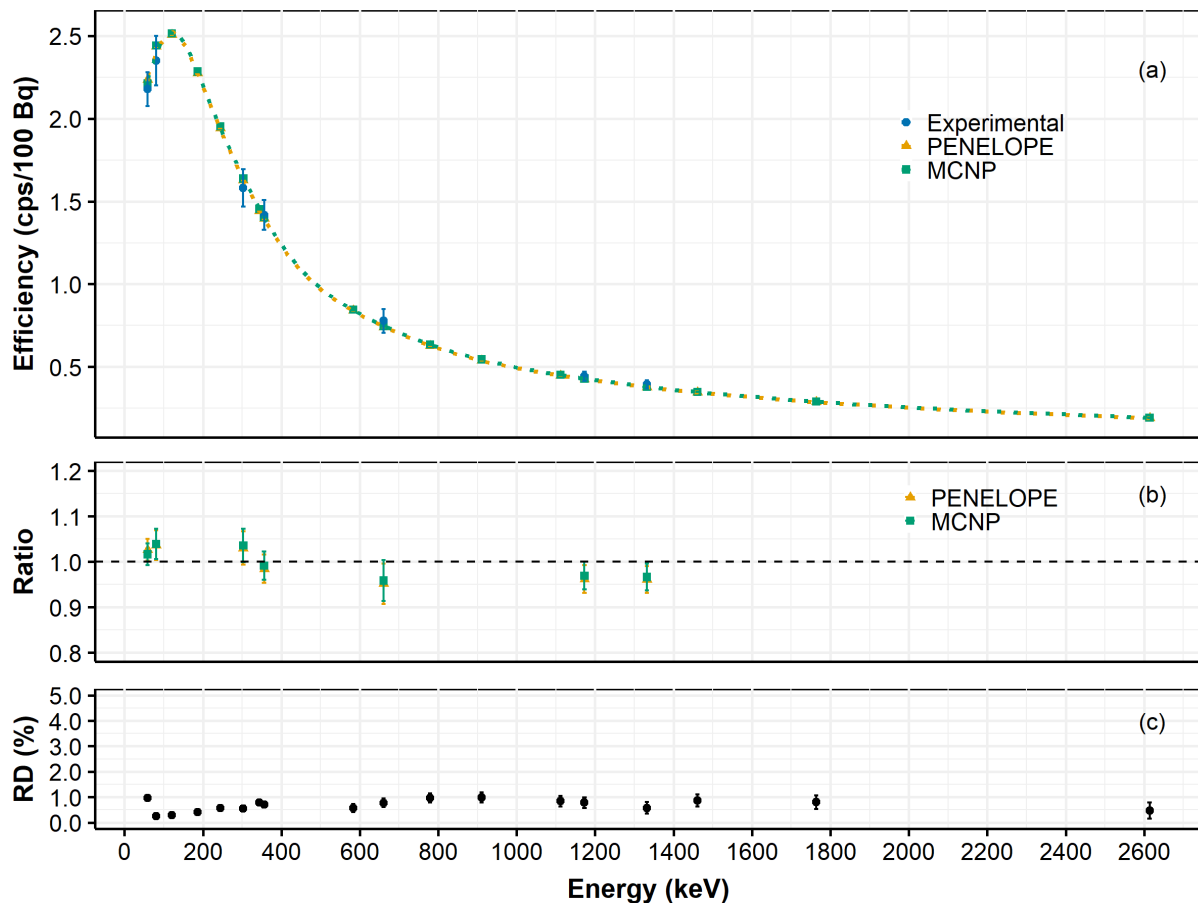


Figure 11. (a) Experimental and simulated FEPEs from PENELOPE and MCNP, (b) ratio of experimental and simulated FEPEs, and (c) relative difference (RD) between the FEPEs from PENELOPE and MCNP for extended sources.

3.2.2. Sources on the side of the detector housing

The simulated and experimental FEPEs for point sources at 0, 5 and 10 cm from the side of the detector housing are shown in Figure 12, Figure 13 and Figure 14, respectively. It was observed that the expanded uncertainty of experimental FEPEs covered simulated FEPEs in all but one cases. The experimental FEPE for 59 keV photon energy at 10 cm distance was 11% higher than the simulated one (Figure 14 (b)). This overestimation of experimental FEPE can be due to the error in positioning the source and the high background in the peak area. Most of the zeta scores were also within the acceptable limit (panel (5), (6) and (7) in Figure 8). The relative difference between the FEPEs from the two codes was in most cases less than 1% (Figure 12(c), Figure 13(c) and Figure 14(c)). Overall, for point sources at the side of the detector, the simulated FEPEs were also in good agreement with experimental FEPEs as their mean relative difference was less than 5% in both Penelope ($2.83\% \pm 2.25\%$) and MCNP ($2.70\% \pm 2.23\%$).

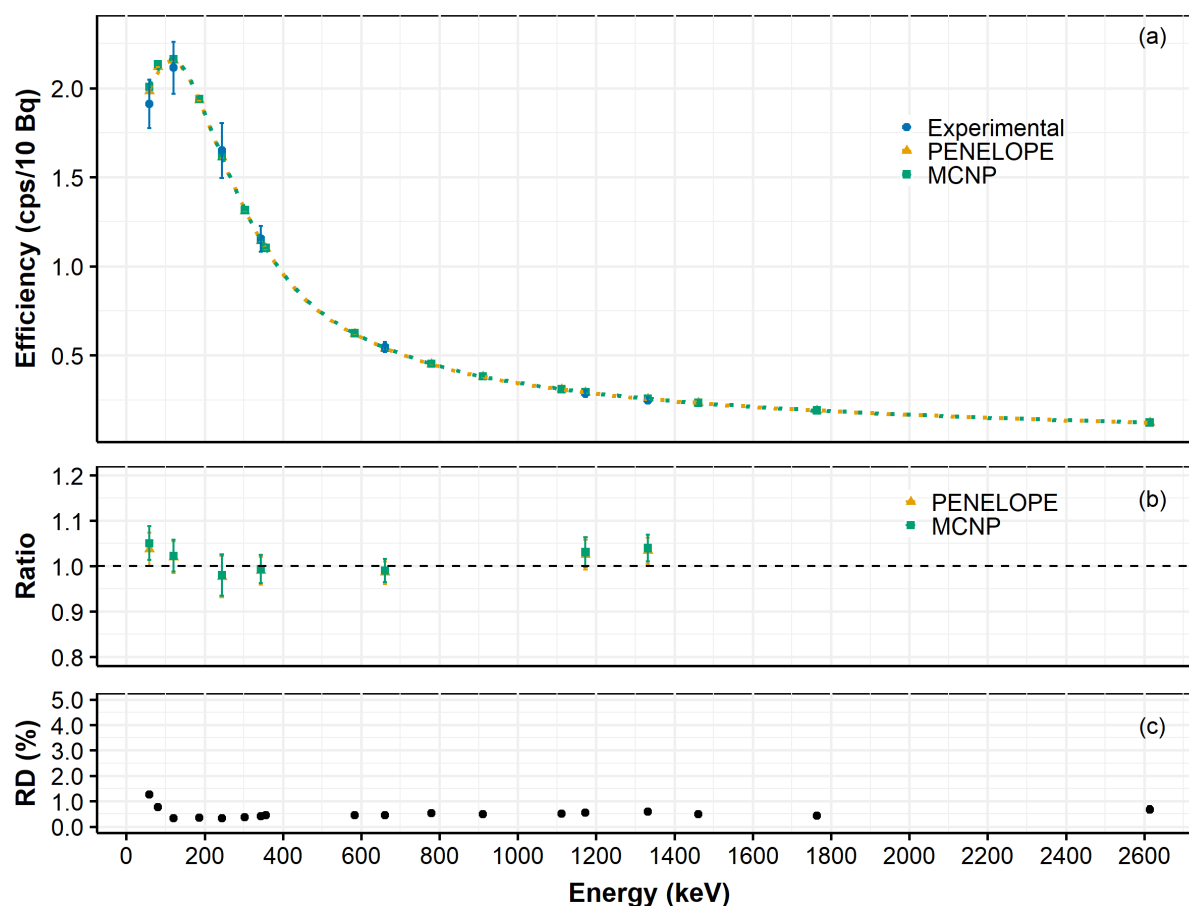


Figure 12. (a) Experimental and simulated FEPEs from PENELOPE and MCNP, (b) ratio of experimental and simulated FEPEs, and (c) relative difference (RD) between the FEPEs from PENELOPE and MCNP for point sources located on the side (0 cm) of the detector housing.

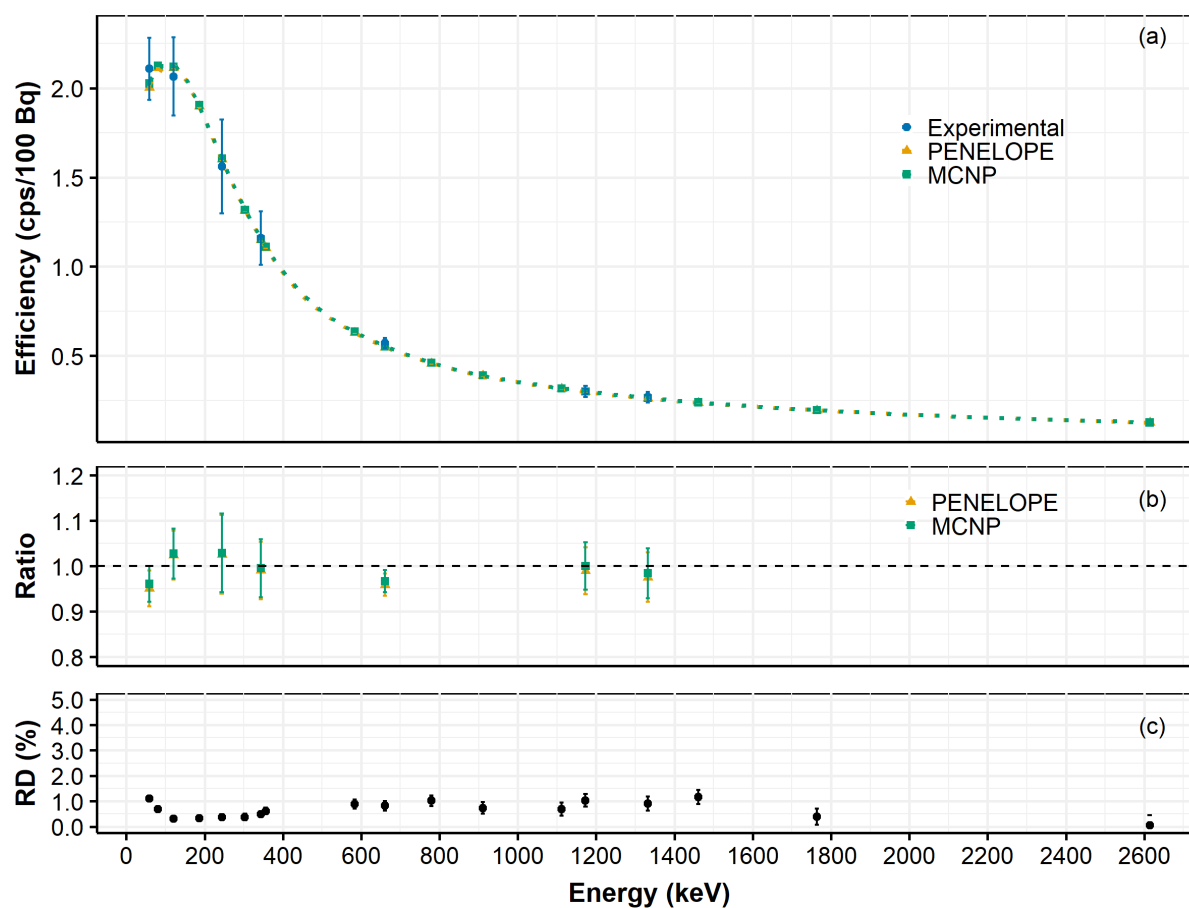


Figure 13. (a) Experimental and simulated FEPEs from PENELOPE and MCNP, (b) ratio of experimental and simulated FEPEs, and (c) relative difference (RD) between the FEPEs from PENELOPE and MCNP for point sources at 5 cm from the side of the detector housing.

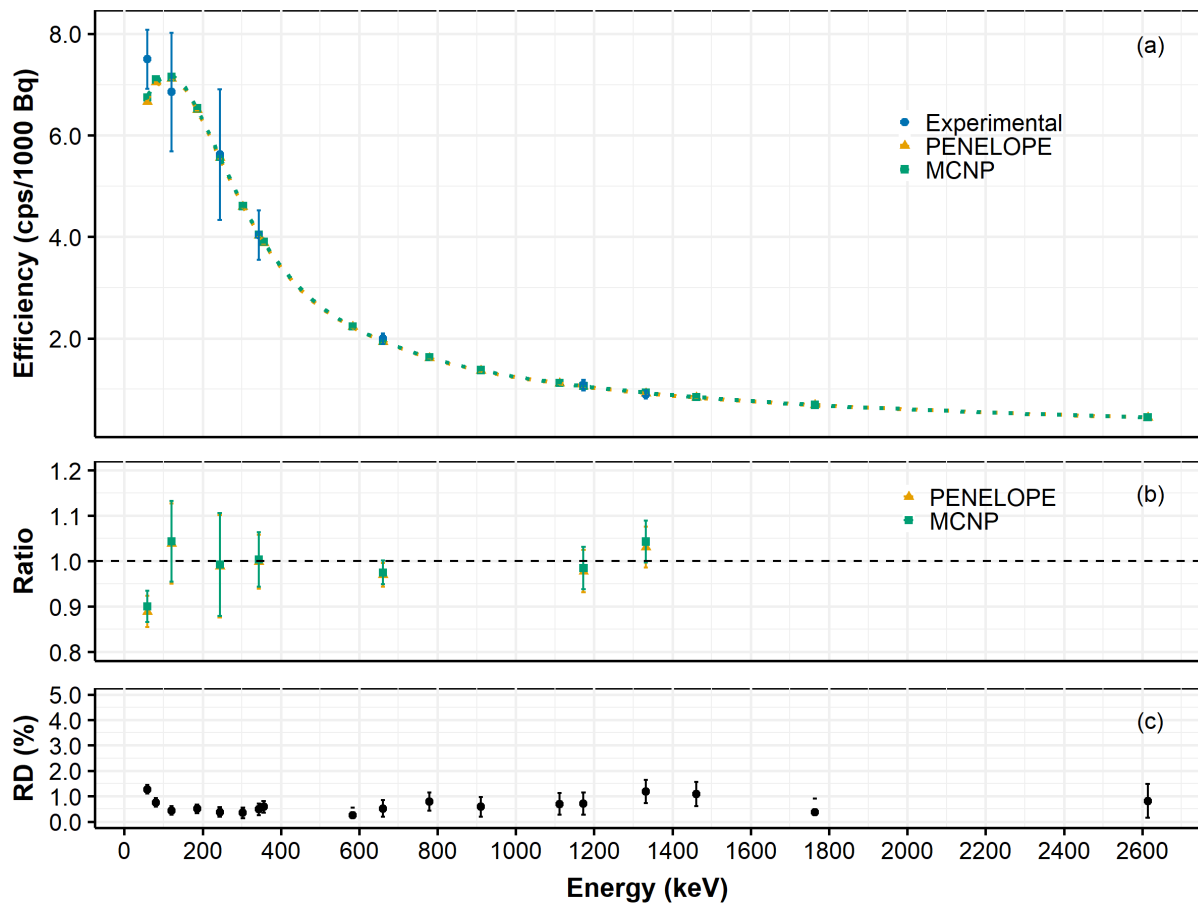


Figure 14. (a) Experimental and simulated FEPEs from PENELOPE and MCNP, (b) ratio of experimental and simulated FEPEs, and (c) relative difference (RD) between the FEPEs from PENELOPE and MCNP for point sources at 10 cm from the side of the detector housing.

3.2.3. *In situ scenario*

The simulated FEPEs for different photon energies for a surface source on a concrete slab (in situ setup) were also calculated separately using PENELOPE and MCNP. The simulated and experimental FEPEs, their ratio and the relative difference between the PENELOPE and MCNP values are shown in Figure 15 (a), (b) and (c), respectively. The expanded uncertainty of two experimental FEPEs (356 and 661 keV) covered the simulated FEPEs (Figure 15 (a) and (b)), and the zeta scores were within the acceptable limit (panel (8) in Figure 8). The simulated FEPEs increased with energy up to about 100 keV and then decreased exponentially in both codes (Figure 15 (a)). In all the cases, the differences were less than 5% between PENELOPE and MCNP simulations. Overall, a good agreement was observed between the experimental and simulated FEPEs for an in situ setup, and the detector model can reliably be used to calculate the FEPEs for such setup. Boson et al. (2009) also concluded that the Monte Carlo approach is suitable for geometries that are difficult to handle by the semi-empirical calibration means.

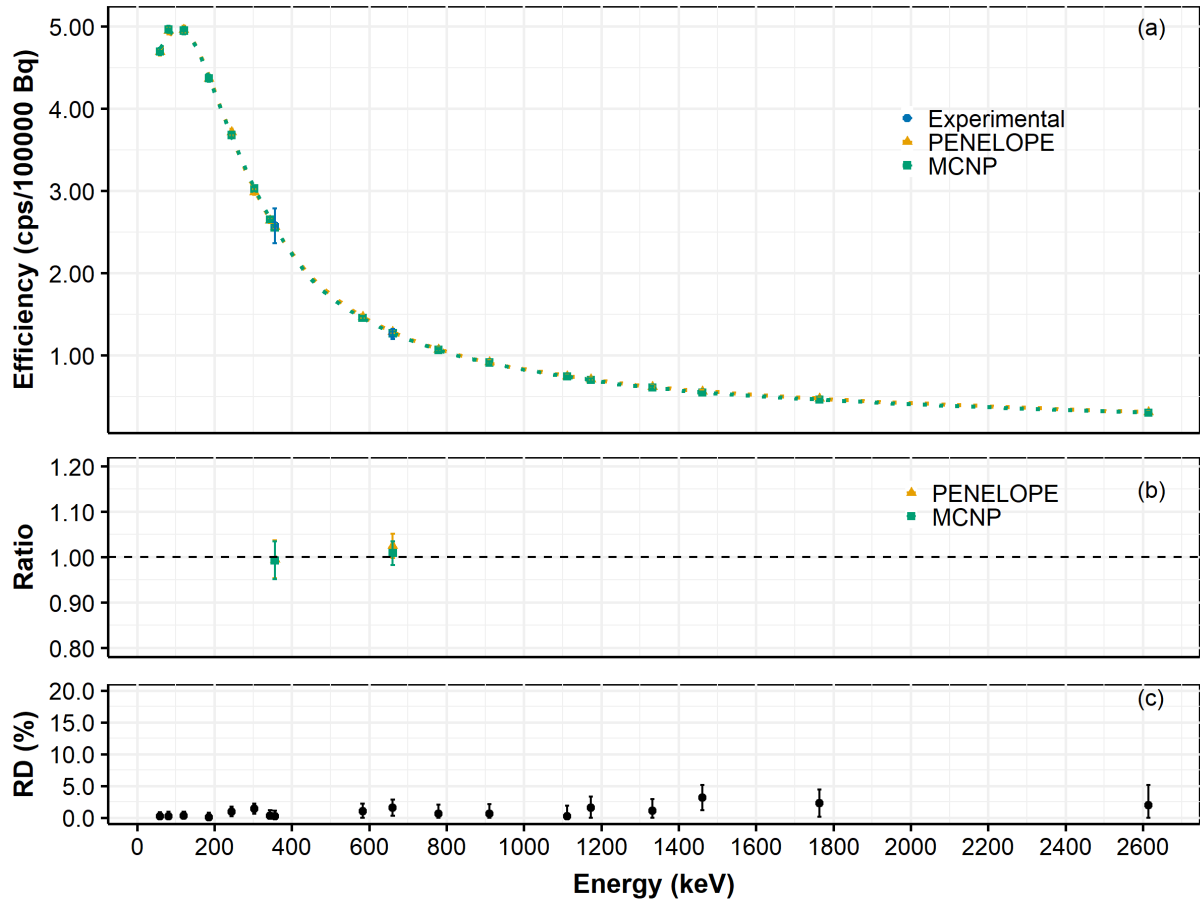


Figure 15. (a) Experimental and simulated FEPEs from PENELOPE and MCNP, (b) ratio of experimental and simulated FEPEs, and (c) relative difference (RD) between the FEPEs from PENELOPE and MCNP for an in situ measurement scenario.

4. Conclusion

In this study, we optimized and verified a $LaBr_3(Ce)$ scintillation detector model using different types of sources and two different Monte Carlo simulation codes. The detector model was optimized based on experimental point-source FEPEs. The optimized model was then validated using different point, extended and surface sources, where the calculated FEPEs were estimated from Monte Carlo simulations using the PENELOPE and the MCNP codes. During both the optimization and the validation process, good agreement between calculated and experimental FEPEs was obtained. The mean relative difference between simulated and experimental FEPEs was $2.84\% \pm 1.93\%$ and $2.79\% \pm 1.99\%$ for PENELOPE and MCNP simulation, respectively. The largest difference of 11% was observed for 59 keV gamma photons of an ^{241}Am point source at 10 cm from the side of the detector housing. This difference, observed only at low energies, can be due to the self-attenuation process within the source. During validation, in 99% of the cases, the zeta scores were less than 2.58 which is

considered acceptable (Shakhashiro et al., 2008). In most of the comparisons, both codes produced similar results (RD <1%). However, in the case of low energies (< 100 keV) and a large-surface source, there was a relatively larger difference between the two codes. The likely cause of this difference between the two codes is the difference in the electromagnetic physics models of the codes. Finally, we conclude that the detector model has been well characterized, and it can be used for efficiency calibration for an in situ scenario. However, it was only validated for photon energies of 356 and 661 keV for an in situ setup. Therefore, it should be further validated using multiple sources with different energies similar to a real in situ measurement in the field.

Reference

- Agostinelli, S., Allison, J., Amako, K. al, Apostolakis, J., Araujo, H., Arce, P., Asai, M., Axen, D., Banerjee, S., Barrand, G. 2, others, 2003. GEANT4—a simulation toolkit. Nucl. instruments methods Phys. Res. Sect. A Accel. Spectrometers, Detect. Assoc. Equip. 506, 250–303.
- Androulakaki, E.G., Kokkoris, M., Tsabaris, C., Eleftheriou, G., Patiris, D.L., Pappa, F.K., Vlastou, R., 2016. In situ γ -ray spectrometry in the marine environment using full spectrum analysis for natural radionuclides. Appl. Radiat. Isot. 114, 76–86. <https://doi.org/10.1016/j.apradiso.2016.05.008>
- Anil Kumar, G., Mazumdar, I., Gothe, D.A., 2009. Efficiency calibration and simulation of a LaBr₃(Ce) detector in close-geometry. Nucl. Instruments Methods Phys. Res. Sect. A Accel. Spectrometers, Detect. Assoc. Equip. 609, 183–186. <https://doi.org/10.1016/j.nima.2009.08.045>
- Baró, J., Sempau, J., Fernández-Varea, J.M., Salvat, F., 1995. PENELOPE: An algorithm for Monte Carlo simulation of the penetration and energy loss of electrons and positrons in matter. Nucl. Inst. Methods Phys. Res. B 100, 31–46. [https://doi.org/10.1016/0168-583X\(95\)00349-5](https://doi.org/10.1016/0168-583X(95)00349-5)
- Bé, M.-M., Chisté, V., Dulieu, C., Browne, E., Baglin, C., Chechev, V., Kuzmenco, N., Helmer, R., Kondev, F., MacMahon, T.D., Lee, K.B., 2006. Table of Radionuclides (Vol. 3 – A = 3 to 244), Monographie BIPM-5. Bureau International Des Poids Et Mesures.
- Bé, M.-M., Chisté, V., Dulieu, C., Mougeot, X., Browne, E., Chechev, V., Kuzmenko, N.,

519 Kondev, F., Luca, A., Galan, M., others, 2010. Table of radionuclides (Vol. 5-A= 22 to
520 244).

521 BNC, 2007. Instruction Manual Model 940 SAM Eagle TM.

522 Boson, J., Plamboeck, A.H., Ramebäck, H., Ågren, G., Johansson, L., 2009. Evaluation of
523 Monte Carlo-based calibrations of HPGe detectors for in situ gamma-ray spectrometry. J.
524 Environ. Radioact. 100, 935–940. <https://doi.org/10.1016/j.jenvrad.2009.06.006>

525 Bronson, F.L., 2003. Validation of the accuracy of the LabSOCS software for mathematical
526 efficiency calibration of Ge detectors for typical laboratory samples, in: Journal of
527 Radioanalytical and Nuclear Chemistry. pp. 137–141.
528 <https://doi.org/10.1023/A:1022248318741>

529 Canberra, 2017. Model S573 ISOCS Calibration Software Technical Reference Manual.

530 Casanovas, R., Morant, J.J., Salvadó, M., 2012. Energy and resolution calibration of NaI(Tl)
531 and LaBr 3(Ce) scintillators and validation of an EGS5 Monte Carlo user code for
532 efficiency calculations. Nucl. Instruments Methods Phys. Res. Sect. A Accel.
533 Spectrometers, Detect. Assoc. Equip. 675, 78–83.
534 <https://doi.org/10.1016/j.nima.2012.02.006>

535 Chiroasca, A., Suvaia, R., Sima, O., 2013. Monte Carlo simulation by GEANT 4 and
536 GESPECOR of in situ gamma-ray spectrometry measurements. Appl. Radiat. Isot. 81, 87–
537 91. <https://doi.org/10.1016/j.apradiso.2013.03.015>

538 Cinelli, G., Tositti, L., Mostacci, D., Baré, J., 2016. Calibration with MCNP of NaI detector for
539 the determination of natural radioactivity levels in the field. J. Environ. Radioact. 155–
540 156, 31–37. <https://doi.org/10.1016/j.jenvrad.2016.02.009>

541 Ciupek, K., Jednoróg, S., Fujak, M., Szewczak, K., 2014. Evaluation of efficiency for in situ
542 gamma spectrometer based upon cerium-doped lanthanum bromide detector dedicated for
543 environmental radiation monitoring. J. Radioanal. Nucl. Chem. 299, 1345–1350.
544 <https://doi.org/10.1007/s10967-013-2906-z>

545 Daza, M.J., Quintana, B., García-Talavera, M., Fernández, F., 2001. Efficiency calibration of a
546 HPGe detector in the [46.54-2000] keV energy range for the measurement of
547 environmental samples. Nucl. Instruments Methods Phys. Res. Sect. A Accel.
548 Spectrometers, Detect. Assoc. Equip. 470, 520–532. <https://doi.org/10.1016/S0168->

549 9002(01)00798-7

550 Ferrari, A., Sala, P.R., Fasso, A., Ranft, J., Siegen, U., others, 2005. FLUKA: a multi-particle
551 transport code.

552 Garnett, R., Prestwich, W. V, Atanackovic, J., Wong, M., Byun, S.H., 2017. Characterization
553 of a LaBr₃(Ce) detector for gamma-ray spectrometry for CANDU power reactors. Radiat.
554 Meas. 106, 628–631. <https://doi.org/10.1016/j.radmeas.2017.03.042>

555 Gilmore, G., 2008. Practical Gamma-ray Spectrometry Practical Gamma-ray Spectrometry 2nd
556 Edition.

557 Goorley, J., James, M., Booth, T., Brown, F., Bull, J., Cox, L., Durkee, J., Elson, J., Fensin, M.,
558 Forster, R., Hendricks, J., Hughes, H., Johns, R., Kiedrowski, B., Mashnik, S., 2013.
559 MCNP6 User's Manual, Version 1.0, LA-CP-13-00634, Los Alamos National Laboratory.

560 Guerra, J.G., Rubiano, J.G., Winter, G., Guerra, A.G., Alonso, H., Arnedo, M.A., Tejera, A.,
561 Gil, J.M., Rodríguez, R., Martel, P., Bolivar, J.P., 2015. A simple methodology for
562 characterization of germanium coaxial detectors by using Monte Carlo simulation and
563 evolutionary algorithms. J. Environ. Radioact. 149, 8–18.
564 <https://doi.org/10.1016/j.jenvrad.2015.06.017>

565 Guerra, J.G., Rubiano, J.G., Winter, G., Guerra, A.G., Alonso, H., Arnedo, M.A., Tejera, A.,
566 Martel, P., Bolivar, J.P., 2018. Modeling of a HPGe well detector using PENELOPE for
567 the calculation of full energy peak efficiencies for environmental samples. Nucl.
568 Instruments Methods Phys. Res. Sect. A Accel. Spectrometers, Detect. Assoc. Equip. 908,
569 206–214. <https://doi.org/10.1016/j.nima.2018.08.048>

570 Guerra, J.G., Rubiano, J.G., Winter, G., Guerra, A.G., Alonso, H., Arnedo, M.A., Tejera, A.,
571 Martel, P., Bolivar, J.P., 2017. Computational characterization of HPGe detectors usable
572 for a wide variety of source geometries by using Monte Carlo simulation and a multi-
573 objective evolutionary algorithm. Nucl. Instruments Methods Phys. Res. Sect. A Accel.
574 Spectrometers, Detect. Assoc. Equip. 858, 113–122.
575 <https://doi.org/10.1016/j.nima.2017.02.087>

576 Hirayama, H., Namito, Y., Bielajew, A.F., Wilderman, S.J., Michigan, U., Nelson, W.R.,
577 others, 2005. The EGS5 code system.

578 Hurtado, S., Villa, M., 2010. An intercomparison of Monte Carlo codes used for in-situ gamma-

579 ray spectrometry. Radiat. Meas. 45, 923–927.
580 <https://doi.org/10.1016/j.radmeas.2010.06.001>

581 IAEA, 2003. Guidelines for radioelement mapping using gamma ray spectrometry data.

582 Iurian, A.R., Cosma, C., 2014. A practical experimental approach for the determination of
583 gamma-emitting radionuclides in environmental samples. Nucl. Instruments Methods
584 Phys. Res. Sect. A Accel. Spectrometers, Detect. Assoc. Equip. 763, 132–136.
585 <https://doi.org/10.1016/j.nima.2014.06.032>

586 Ji, Y.Y., Lim, T., Hitomi, K., Yajima, T., 2019. Assessment of radioactive cesium deposition
587 using ground-based gamma-ray spectrometry with a LaBr₃(Ce) detector. J. Radiol. Prot.
588 39, 1006–1020. <https://doi.org/10.1088/1361-6498/ab3a9f>

589 Jovanovic, S., Dlabac, A., Mihaljevic, N., 2010. ANGLE v2.1 - New version of the computer
590 code for semiconductor detector gamma-efficiency calculations, in: Nuclear Instruments
591 and Methods in Physics Research, Section A: Accelerators, Spectrometers, Detectors and
592 Associated Equipment. North-Holland, pp. 385–391.
593 <https://doi.org/10.1016/j.nima.2010.02.058>

594 Jung, S., Sung, W., Lee, J., Ye, S.J., 2018. MCNP6.1 simulations for low-energy atomic
595 relaxation: Code-to-code comparison with GATEv7.2, PENELOPE2014, and EGSnrc.
596 Nucl. Instruments Methods Phys. Res. Sect. B Beam Interact. with Mater. Atoms 415,
597 117–126. <https://doi.org/10.1016/j.nimb.2017.11.024>

598 Karfopoulos, K.L., Anagnostakis, M.J., 2010. Parameters affecting full energy peak efficiency
599 determination during Monte Carlo simulation. Appl. Radiat. Isot. 68, 1435–1437.
600 <https://doi.org/10.1016/j.apradiso.2009.11.020>

601 Kastlander, J., Bargholtz, C., 2011. In situ method to determine depth distribution of buried
602 activity. Appl. Radiat. Isot. 69, 773–779. <https://doi.org/10.1016/j.apradiso.2011.01.012>

603 Knoll, G.F., 2010. Radiation Detection and Measurement (4th Edition), John Wiley & Sons,
604 Inc.

605 Mauring, A., Vidmar, T., Gäfvert, T., Drefvelin, J., Fazio, A., 2018. InSiCal – A tool for
606 calculating calibration factors and activity concentrations in in situ gamma spectrometry.
607 J. Environ. Radioact. 188, 58–66. <https://doi.org/10.1016/j.jenvrad.2017.10.011>

608 Milbrath, B.D., Choate, B.J., Fast, J.E., Hensley, W.K., Kouzes, R.T., Schweppe, J.E., 2007.
609 Comparison of LaBr₃:Ce and NaI(Tl) scintillators for radio-isotope identification
610 devices. Nucl. Instruments Methods Phys. Res. Sect. A Accel. Spectrometers, Detect.
611 Assoc. Equip. 572, 774–784. <https://doi.org/10.1016/j.nima.2006.12.003>

612 Miller, K., Shebell, P., 1993. In situ gamma ray spectrometry - a tutorial for scientists.

613 Mouhti, I., Elanique, A., Messous, M.Y., 2017. Monte Carlo modelling of a NaI(Tl) scintillator
614 detectors using MCNP simulation code. J. Mater. Environ. Sci. 8, 4560–4565.
615 <https://doi.org/10.26872/jmes.2017.8.12.481>

616 Mouhti, I., Elanique, A., Messous, M.Y., Belhorma, B., Benahmed, A., 2018. Validation of a
617 NaI(Tl) and LaBr₃ (Ce) detector's models via measurements and Monte Carlo
618 simulations. J. Radiat. Res. Appl. Sci. 11, 335–339.
619 <https://doi.org/10.1016/j.jrras.2018.06.003>

620 MultiSpect, 2018. MultiSpect Analysis.

621 Murphy, N.M., León Vintró, L., Burbidge, C.I., Currivan, L., 2020. An automated programme
622 for the optimisation of HPGe detector parameters using an evolutionary algorithm with
623 GESPECOR. Appl. Radiat. Isot. 156, 108883.
624 <https://doi.org/10.1016/j.apradiso.2019.108883>

625 Nelder, J.A., Mead, R., 1965. A Simplex Method for Function Minimization. Comput. J.
626 <https://doi.org/10.1093/comjnl/7.4.308>

627 Ordóñez, J., Gallardo, S., Ortiz, J., Sáez-Muñoz, M., Martorell, S., 2019. Intercomparison of
628 full energy peak efficiency curves for an HPGe detector using MCNP6 and GEANT4.
629 Radiat. Phys. Chem. 155, 248–251. <https://doi.org/10.1016/j.radphyschem.2018.06.049>

630 Python, 2020. Python: A dynamic, open source programming language.

631 Rizwan, U., Chester, A., Domingo, T., Starosta, K., Williams, J., Voss, P., 2015. A method for
632 establishing absolute full-energy peak efficiency and its confidence interval for HPGe
633 detectors. Nucl. Instruments Methods Phys. Res. Sect. A Accel. Spectrometers, Detect.
634 Assoc. Equip. 802, 102–112A. <https://doi.org/10.1016/j.nima.2015.08.071>

635 Rostron, P.D., Heathcote, J.A., Ramsey, M.H., 2014. Comparison between in situ and ex situ
636 gamma measurements on land areas within a decommissioning nuclear site: A case study

637 at Dounreay. J. Radiol. Prot. 34, 495–508. <https://doi.org/10.1088/0952-4746/34/3/495>

638 Sabbatucci, L., Salvat, F., 2016. Theory and calculation of the atomic photoeffect. Radiat. Phys.
 639 Chem. <https://doi.org/10.1016/j.radphyschem.2015.10.021>

640 Sahiner, H., Liu, X., 2020. Gamma spectral analysis by artificial neural network coupled with
 641 Monte Carlo simulations. Nucl. Instruments Methods Phys. Res. Sect. A Accel.
 642 Spectrometers, Detect. Assoc. Equip. 953, 163062.
 643 <https://doi.org/10.1016/j.nima.2019.163062>

644 Saint-Gobain, 2020. Standard Scintillation Product List | Saint-Gobain Crystals [WWW
 645 Document]. URL [https://www.crystals.saint-gobain.com/products/radiation-detection-](https://www.crystals.saint-gobain.com/products/radiation-detection-products/standard-scintillation-product-list)
 646 [products/standard-scintillation-product-list](https://www.crystals.saint-gobain.com/products/radiation-detection-products/standard-scintillation-product-list) (accessed 11.8.20).

647 Saizu, M.A., Cata-Danil, G., 2011. Lanthanum bromide scintillation detector for gamma
 648 spectrometry applied in internal radioactive contamination measurements. UPB Sci. Bull.
 649 Ser. A Appl. Math. Phys.

650 Salgado, C.M., Brandão, L.E.B., Schirru, R., Pereira, C.M.N.A., Conti, C.C., 2012. Validation
 651 of a NaI(Tl) detector's model developed with MCNP-X code. Prog. Nucl. Energy 59, 19–
 652 25. <https://doi.org/10.1016/j.pnucene.2012.03.006>

653 Salvat, F., 2019. PENELOPE 2018: A code system for Monte Carlo simulation of electron and
 654 photon transport. OECD. [https://doi.org/https://doi.org/https://doi.org/10.1787/32da5043-](https://doi.org/https://doi.org/https://doi.org/10.1787/32da5043-en)
 655 [en](https://doi.org/https://doi.org/https://doi.org/10.1787/32da5043-en)

656 Scofield, J.H., 1973. Theoretical photoionization cross sections from 1 to 1500 keV. Livermore,
 657 Calif.

658 Shakhashiro, A., Trinkl, A., Sansone, U., 2008. The IAEA's "ALMERA Network" proficiency
 659 test on the determination of gamma-emitting radionuclides: A test of results comparability.
 660 Appl. Radiat. Isot. 66, 1722–1725. <https://doi.org/10.1016/j.apradiso.2007.10.021>

661 Shizuma, K., Oba, Y., Takada, M., 2016. A practical method for determining γ -ray full-energy
 662 peak efficiency considering coincidence-summing and self-absorption corrections for the
 663 measurement of environmental samples after the Fukushima reactor accident. Nucl.
 664 Instruments Methods Phys. Res. Sect. B Beam Interact. with Mater. Atoms 383, 183–190.
 665 <https://doi.org/10.1016/j.nimb.2016.06.019>

666 Su, G., Zeng, Z., Cheng, J., 2011. Monte carlo simulation of in situ LaBr gamma-ray
667 spectrometer for marine environmental monitoring. *Radiat. Prot. Dosimetry* 146, 103–106.
668 <https://doi.org/10.1093/rpd/ncr122>

669 Tain, J.L., Agramunt, J., Algora, A., Aprahamian, A., Cano-Ott, D., Fraile, L.M., Guerrero, C.,
670 Jordan, M.D., Mach, H., Martinez, T., Mendoza, E., Mosconi, M., Nolte, R., 2015. The
671 sensitivity of LaBr₃:Ce scintillation detectors to low energy neutrons: Measurement and
672 Monte Carlo simulation. *Nucl. Instruments Methods Phys. Res. Sect. A Accel.*
673 *Spectrometers, Detect. Assoc. Equip.* 774, 17–24.
674 <https://doi.org/10.1016/j.nima.2014.11.060>

675 Tang, X. Bin, Meng, J., Wang, P., Cao, Y., Huang, X., Wen, L.S., Chen, D., 2016. Simulated
676 minimum detectable activity concentration (MDAC) for a real-time UAV airborne
677 radioactivity monitoring system with HPGe and LaBr₃ detectors. *Radiat. Meas.* 85, 126–
678 133. <https://doi.org/10.1016/j.radmeas.2015.12.031>

679 Tyler, A.N., 2008. In situ and airborne gamma-ray spectrometry. *Radioact. Environ.* 11, 407–
680 448. [https://doi.org/10.1016/S1569-4860\(07\)11013-5](https://doi.org/10.1016/S1569-4860(07)11013-5)

681 Urban, T., Vágner, P., 2019. Simulation of the response of a LaBr₃(Ce) detector in an
682 atmosphere contaminated with radionuclides after a nuclear power plant accident. *Radiat.*
683 *Prot. Dosimetry* 186, 346–350. <https://doi.org/10.1093/rpd/ncz259>

684 Van Loef, E. V.D., Dorenbos, P., Van Eijk, C.W.E., Krämer, K.W., Güdel, H.U., 2002.
685 Scintillation properties of LaBr₃:Ce³⁺ crystals: Fast, efficient and high-energy-resolution
686 scintillators, in: *Nuclear Instruments and Methods in Physics Research, Section A:*
687 *Accelerators, Spectrometers, Detectors and Associated Equipment.*
688 [https://doi.org/10.1016/S0168-9002\(02\)00712-X](https://doi.org/10.1016/S0168-9002(02)00712-X)

689 Van Rossum, G., Drake, F.L., 2011. The python language reference manual. Network Theory
690 Ltd.

691 Varley, A., Tyler, A., Dowdall, M., Bondar, Y., Zabrotski, V., 2017. An in situ method for the
692 high resolution mapping of ¹³⁷Cs and estimation of vertical depth penetration in a highly
693 contaminated environment. *Sci. Total Environ.* 605–606, 957–966.
694 <https://doi.org/10.1016/j.scitotenv.2017.06.067>

695 Varley, A., Tyler, A., Smith, L., Dale, P., Davies, M., 2015. Remediating radium contaminated

696 legacy sites: Advances made through machine learning in routine monitoring of “hot”
697 particles. Sci. Total Environ. 521–522, 270–279.
698 <https://doi.org/10.1016/j.scitotenv.2015.03.131>

699 Vidmar, T., Aubineau-Laniece, I., Anagnostakis, M.J., Arnold, D., Brettner-Messler, R.,
700 Budjas, D., Capogni, M., Dias, M.S., De Geer, L.E., Fazio, A., Gasparro, J., Hult, M.,
701 Hurtado, S., Jurado Vargas, M., Laubenstein, M., Lee, K.B., Lee, Y.K., Lepy, M.C.,
702 Maringer, F.J., Medina Peyres, V., Mille, M., Morales, M., Nour, S., Plenteda, R., Rubio
703 Montero, M.P., Sima, O., Tomei, C., Vidmar, G., 2008. An intercomparison of Monte
704 Carlo codes used in gamma-ray spectrometry. Appl. Radiat. Isot. 66, 764–768.
705 <https://doi.org/10.1016/j.apradiso.2008.02.015>

706 Vidmar, T., Kanisch, G., Vidmar, G., 2011. Calculation of true coincidence summing
707 corrections for extended sources with EFFTRAN. Appl. Radiat. Isot. 69, 908–911.
708 <https://doi.org/10.1016/j.apradiso.2011.02.042>

709 Virtanen, P., Gommers, R., Oliphant, T.E., Haberland, M., Reddy, T., Cournapeau, D.,
710 Burovski, E., Peterson, P., Weckesser, W., Bright, J., van der Walt, S.J., Brett, M., Wilson,
711 J., Millman, K.J., Mayorov, N., Nelson, A.R.J., Jones, E., Kern, R., Larson, E., Carey,
712 C.J., Polat, İ., Feng, Y., Moore, E.W., VanderPlas, J., Laxalde, D., Perktold, J., Cimrman,
713 R., Henriksen, I., Quintero, E.A., Harris, C.R., Archibald, A.M., Ribeiro, A.H., Pedregosa,
714 F., van Mulbregt, P., Vijaykumar, A., Bardelli, A. Pietro, Rothberg, A., Hilboll, A.,
715 Kloeckner, A., Scopatz, A., Lee, A., Rokem, A., Woods, C.N., Fulton, C., Masson, C.,
716 Häggström, C., Fitzgerald, C., Nicholson, D.A., Hagen, D.R., Pasechnik, D. V., Olivetti,
717 E., Martin, E., Wieser, E., Silva, F., Lenders, F., Wilhelm, F., Young, G., Price, G.A.,
718 Ingold, G.L., Allen, G.E., Lee, G.R., Audren, H., Probst, I., Dietrich, J.P., Silterra, J.,
719 Webber, J.T., Slavič, J., Nothman, J., Buchner, J., Kulick, J., Schönberger, J.L., de
720 Miranda Cardoso, J.V., Reimer, J., Harrington, J., Rodríguez, J.L.C., Nunez-Iglesias, J.,
721 Kuczynski, J., Tritz, K., Thoma, M., Newville, M., Kümmerer, M., Bolingbroke, M.,
722 Tartre, M., Pak, M., Smith, N.J., Nowaczyk, N., Shebanov, N., Pavlyk, O., Brodtkorb,
723 P.A., Lee, P., McGibbon, R.T., Feldbauer, R., Lewis, S., Tygier, S., Sievert, S., Vigna, S.,
724 Peterson, S., More, S., Pudlik, T., Oshima, T., Pingel, T.J., Robitaille, T.P., Spura, T.,
725 Jones, T.R., Cera, T., Leslie, T., Zito, T., Krauss, T., Upadhyay, U., Halchenko, Y.O.,
726 Vázquez-Baeza, Y., 2020. SciPy 1.0: fundamental algorithms for scientific computing in
727 Python. Nat. Methods. <https://doi.org/10.1038/s41592-019-0686-2>

728 Werner, C J, Armstrong, J., Brown, F.B., Bull, J.S., Casswell, L., Cox, L.J., Dixon, D., Forster,
 729 R.A., Goorley, J.T., Hughes, H.G., Favorite, J., Martz, R., Mashnik, S.G., Rising, M.E.,
 730 Solomon, C., Sood, A., Sweezy, J.E., Werner, Christopher J., Zukaitis, A., Anderson, C.,
 731 Elson, J.S., Durkee, J.W., Johns, R.C., McKinney, G.W., McMath, G.E., Hendricks, J.S.,
 732 Pelowitz, D.B., Prael, R.E., Booth, T.E., James, M.R., Fensin, M.L., Wilcox, T.A.,
 733 Kiedrowski, B.C., 2017. MCNP User's Manual Code Version 6.2, Los Alamos National
 734 Laboratory.

735 White, M.C., 2012. Further Notes on MCPLIB03/04 and New MCPLIB63/84 Compton
 736 Broadening Data For All Versions of MCNP5, Los Alamos National Laboratory Report
 737 No. LA-UR-12-00018.

738 Wu, Y., Tang, B., 2012. Monte-Carlo simulation of response functions for natural gamma-rays
 739 in LaBr 3 detector system with complex borehole configurations, in: Plasma Science and
 740 Technology. pp. 481–487. <https://doi.org/10.1088/1009-0630/14/6/10>

741 Zeng, Z., Pan, X., Ma, H., He, J., Cang, J., Zeng, M., Mi, Y., Cheng, J., 2017. Optimization of
 742 an underwater in-situ LaBr₃:Ce spectrometer with energy self-calibration and efficiency
 743 calibration. Appl. Radiat. Isot. 121, 101–108.
 744 <https://doi.org/10.1016/j.apradiso.2016.12.016>

745 Zhang, Yingying, Li, C., Liu, D., Zhang, Ying, Liu, Y., 2015. Monte Carlo simulation of a
 746 NaI(Tl) detector for in situ radioactivity measurements in the marine environment. Appl.
 747 Radiat. Isot. 98, 44–48. <https://doi.org/10.1016/j.apradiso.2015.01.009>

748